Cement and Concrete Research 128 (2020) 105940

Contents lists available at ScienceDirect

Cement and Concrete Research

journal homepage: www.elsevier.com/locate/cemconres

Influence of low curing temperatures on the tensile response of low clinker strain hardening UHPFRC under full restraint

Mohamed Abdul Hafiz[a,*], Jørgen Skibsted[b], Emmanuel Denarié[a]

[a] Laboratory of Maintenance and Safety of Structures, MCS-IIC-ENAC, EPFL - Ecole Polytechnique Fédérale de Lausanne, , CH–1015 Lausanne, Switzerland
[b] Department of Chemistry and Interdisciplinary Nanoscience Center (iNANO), Aarhus University, Langelandsgade 140, DK-8000 Aarhus C, Denmark

ARTICLE INFO

Keywords:
UHPFRC
Low curing temperature
Solid state ^{29}Si MAS NMR
Autogenous shrinkage
Eigenstresses under full restraint

ABSTRACT

The tensile response of strain hardening UHPFRC under full restraint, subjected to curing temperatures of 20 °C, 10 °C, 5 °C, was investigated for two types of mixes with silica fume; Mix I with pure type I cement and Mix II with 50% replacement of cement with limestone filler, both having a similar steel fibrous mix. The development of the elastic modulus, tensile strength, autogenous shrinkage and eigenstresses were put into perspective with the hydration kinetics. Two phases of pozzolanic reaction with different rates of consumption of silica fume were identified. A systematic increase of the autogenous shrinkage and eigenstresses with the curing temperatures was observed. The eigenstresses development was much slower in the case of Mix II, owing to its larger relaxation potential. The eigenstresses in Mix I reached the strain hardening domain after one month, whereas the same in Mix II were only approaching the strain hardening domain after three months.

1. Introduction

Strain Hardening Ultra High Performance Fiber Reinforced Concretes (SH-UHPFRC) are very well adapted for rehabilitation or reinforcement (combined with rebars) applications of reinforced concrete structures because of their optimal properties (high tensile strength, over 12 MPa, significant strain hardening, up to 5‰, very low permeability to liquids and gases, and outstanding durability) [1–3]. When a new layer of UHPFRC is applied on an existing structure, early age deformations and drying shrinkage (upon final exposure of the UHPFRC free surfaces), lead to the development of tensile eigenstresses in the UHPFRC. The eigenstresses can reach high stress levels at early age, and might develop further over the long term in the case of drying shrinkage, for mixes where the latter dominates over the autogenous deformations (such as mixes without silica fume). More generally, a major motivation to use Strain Hardening UHPFRC in structures is to make use of their potential under tensile loading, with tensile stresses at serviceability (under eigenstresses, live loads and deadweight) as high as possible, still preserving their outstanding protective properties. As such, an in-depth understanding of the factors governing the development of eigenstresses and their interaction with the tensile resistance and deformability envelope of these materials is of major importance.

The resistance and deformability offered by UHPFRC is age as well as temperature and moisture curing dependent [4–9]. It also depends to a large extend on the orientation of the fibers in the practical applications [3]. Strain Hardening UHPFRC with a constant tensile response under any situation of application, is an idealistic vision. A more realistic goal is to have “robust” mixes that exhibit a tensile hardening response in a wide range of applications, such as that classified in the French standard as “strongly hardening – T3” after material tests characterizations [10]. However, even the best mix in the lab, if improperly placed, with an inappropriate workability, or in confined conditions with too narrow rebar spacing or clearance with formwork surfaces can lose its strain hardening character and lead to premature cracking, compromising the expected protective properties that motivate its use. The knowledge about the development of the tensile resistance and deformability properties like stiffness, elastic modulus and post elastic limit deformability under low temperature curing conditions for UHPFRC materials, is very scarce in literature [11].

The magnitude and development of eigenstresses in cast-on site applications depend on structural factors (restraint governed by the relative stiffness of new layer and substrate as well as boundary conditions – static system and support of the substrate), and material related factors of the new layer (development of microstructure and pore structure, ageing elastic and viscoelastic properties, autogenous deformations, drying shrinkage). These factors can be related to the hydration kinetics of the binders and external curing and long term ambient conditions [12,13].

* Corresponding author.
E-mail address: mohamed.hafiz@epfl.ch (M.A. Hafiz).

https://doi.org/10.1016/j.cemconres.2019.105940
Received 24 June 2019; Received in revised form 27 September 2019; Accepted 13 November 2019

The influence of curing temperatures on the kinetics of the development of eigenstresses, especially the effect of low temperatures representative of in-situ casting conditions in winter, are not very well understood for UHPFRC materials [5,14,15]. Very few works have been carried out to study restrained shrinkage and the associated eigenstresses development in UHPC [16,17] and in UHPFRC [4,5,14,18–21]. Some works has also been carried out under non-isothermal conditions, with the temperature varying according to the development of heat of hydration in the UHPFRC mixes [5,22]. However, to the best of the authors' knowledge, no extensive research has been reported in open literature on the influence of full restraint conditions on the development of the eigenstresses in UHPFRC, under low temperatures. Moreover, studies on the development of autogenous deformations and eigenstresses under restraint for UHPFRC mixes with massive replacement of clinker with limestone fillers are very scarce [21,23].

Many authors showed that the autogenous shrinkage in cementitious materials is driven by capillary stresses that develop in the pore structure due to the decrease of relative humidity as the hydration progresses in systems with partial hydration of binders [24–30]. The capillary stresses, which can be represented by the Kelvin-Laplace equations, are temperature dependent and as such, many studies [14,28,29,31,32] have shown that the autogenous deformations cannot be represented using a maturity function unlike the other macro mechanical properties like compressive strength and elastic modulus [14]. Many studies have been carried out to understand the effect of curing temperatures on the development of autogenous shrinkage in cement based materials [25,29,31,33]. However, very few investigations have considered the same effect for HPC [34,35], UHPC [15,36] or UHPFRC [5,7,8,14]. Moreover, most of these studies focus on curing temperatures higher than 20 °C and investigations on the effect of curing temperatures lower than 20 °C is very scarce [14,15].

Curing temperatures affect the development of the microstructure and the pore network in cementitious materials, which in turn affect the induced capillary stresses and the associated autogenous shrinkage. Many studies have shown that, even though the rate of hydration is much slower at lower curing temperatures, the developed microstructure at a later age has a more uniform distribution of the hydration products, with lesser pores [37–43]. However, there is a disagreement in the ultimate degree of hydration at different temperatures. While many studies show that the ultimate degree of hydration is higher when the curing temperature is lower [38,40,41,44], some others show that the ultimate degree of hydration remain the same at different curing temperatures [37].

The viscoelastic properties of the solid skeleton help in mitigating the development of eigenstresses in cementitious materials. Very few studies have been carried out to investigate the viscoelastic behavior of UHPFRC in compression [4,27,45–49] and in tension [6,18,48,50–55], especially at early age. The compressive creep response of UHPFRC is significantly lower than that of ordinary concretes at a similar loading age and load level [56]. The basic compressive creep coefficient of UHPFRC without thermal treatment, at a loading age of 28 days, for a load level below 40% of the compressive strength, is typically 0.8–1, instead of 2–4 for normal concretes [56]. Not many works have been carried out to study the viscous response of UHPFRC mixes with partial replacement of cement clinker with supplementary cementitious materials. However, similar studies on cementitious materials other than UHPFRC mixes, report contradictory viscous responses. On the one hand, many authors have reported an increase in the creep response in mixes with partial replacement of cement clinker with fly ash [57–60], blast furnace slag [58–60] or limestone filler [57]. On the other hand, some others have reported a decrease in the creep response in mixes with fly ash [61–64] and Ground Granulated Blast Furnace Slag [61]. However, it should be noted that the observed trends of the viscous response in all these studies were very dependent on the age of loading. In short, the viscous response of mixes with SCM, especially that of UHPFRC mixes, is not fully understood.

Moreover, except the investigations in [11], no studies have reported the development with age of tensile resistance parameters like strength and deformability under low temperatures for UHPFRC mixes. Fundamental research is needed in this field to make sure that the eigenstresses developed under these curing conditions are lower than the resistance of the material, in order to meet the required serviceability and durability criteria, or to study the couplings between the development of eigenstresses and the tensile hardening response.

This paper investigates the influence of moderate to low curing temperatures, 20 °C, 10 °C and 5 °C, on the development of mechanical properties (elastic modulus and tensile strength), autogenous shrinkage and associated eigenstresses under full restraint, for two types of SH-UHPFRC mixes. Mix I with pure type I cement, silica fume and steel fibers and Mix II with 50% replacement of cement with limestone filler and a similar steel fibrous mix.

In a first step, the kinetics of hydration of the two mixes are characterized by means of isothermal calorimetry and ^{29}Si MAS NMR to determine the evolution of the overall degree of hydration, the activation energies of the mixes, and the degree of hydration of cement and degree of reaction of silica fume with age. The development of elastic modulus, autogenous deformations and eigenstresses with age, maturity and degree of hydration are then presented and discussed. Finally, the structural response of the materials, represented by the development of autogenous shrinkage and eigenstresses under full restraint, is classified into three domains. The domains are put into perspective with the material level of kinetics of hydration and reaction of the binders and evolution of elastic modulus, taking into consideration the evolution of the resistance of the two materials at different ages and for different curing temperatures.

2. Experimental

2.1. Materials

Two types of SH-UHPFRC mixes were used in the present study; Mix I and Mix II, both from the CEMTEC$_{multiscale}$© family, which were initially developed at Laboratoire Central des Ponts et Chaussées (LCPC), France [65]. These mixes were optimized and modified in the framework of the research works held in MCS/EPFL for rehabilitation and strengthening of existing structures [66,67]. Mix I was a SH-UHPFRC of type CM22_TKK_b, composed of an ultracompact cementitious matrix containing cement (type CEM I 52.5 HTS from Le Teil, Lafarge), white microsilica (SEPR, BET = 14 m^2/g), superplasticizer (Zementol Zeta Super S from TKK, Slovenia) and water. However, since the degree of hydration of Mix I was only about 28–30% after one month [14,21], 50% of the cement in Mix I could advantageously be replaced with two types of inert limestone fillers: Betoflow D® and Betocarb SL® (OMYA), of different gradings, to produce Mix II, which is a UHPFRC of type CM22_TKK_LF, with improved sustainability. Both mixes had a fibrous mix containing two types of steel fibers; microfibers and macrofibers, with a total dosage of 9% by volume after the concepts developed by Rossi et al. [65]. The detailed compositions of Mix I and II are given in Table 1 where the compositions of the mixes with fibers (Mix I, Mix II) and that of the UHPC matrix without fibers (Mix I$_m$ and Mix II$_m$) are shown. Table 2 shows the tests that were carried out only on the UHPC matrix and those conducted on the UHPFRC mixes.

The properties in the hardened state and fresh state are given in Table 3 and Table 4, respectively. The compressive strength and modulus of elasticity were determined on 70 mm × 140 mm cylinders, whereas the tensile properties were obtained from uniaxial tensile tests at a strain rate of 10^{-5} 1/s, on dumbbell specimens with a center cross section of 50 mm × 30 mm, following [68]. The sorptivity was also measured for both mixes at an age of 28 days following EN 1925: 99-07. More details regarding the mechanical properties and the chemical composition of the components could be found in [21].

Table 1
Compositions of mixes I and II.

Material	Mix I	Mix II	Mix I_m*	Mix II_m*
	[kg/m^3]	[kg/m^3]	[kg/m^3]	[kg/m^3]
Cement, CEM I 52.5 le Teil	1467.0	733.7	1616.2	809.6
Silica fume, SEPR	381.4	293.5	420.2	323.8
Limestone filler 1 (Betocarb SL®)	–	223.0	–	246.1
Limestone filler 2 (Betoflow D®)	–	510.6	–	563.4
Steel fibers (straight macro fibers; l_f = 10 mm, d_f = 0.2 mm and microfibers/steel wool)	706.5	706.5	–	–
Total water	225.8	217.9	248.7	240.4
Superplasticizer from TKK, Slovenia; Zementol zeta super S; polycarboxylate; 25% solid content; (total amount)	20.5	14.7	22.6	16.2

* Corresponds to the compositions of the UHPC matrix without fibers.

Table 2
Type of mixes used for different tests.

Mix used	Type of test
UHPFRC - Mix I, Mix II	Elastic modulus – Vibration Resonance Frequency tests (VRFT)
	Autogenous deformations – Temperature Stress Testing Machine (TSTM)
	Eigenstresses development – TSTM
	Uniaxial tensile tests
UHPC - Mix I_m, Mix II_m	Isothermal calorimetry
	^{29}Si MAS NMR tests

2.2. Isothermal calorimetry tests

Isothermal calorimetry tests were performed in a TAM AIR calorimeter from TA instruments, and the heat flow in the mixes was continuously measured from the time of casting. The thermostat in the TAM AIR can maintain the temperature in the samples and the surrounding environment within ± 0.02 °C of the chosen isothermal temperature. The mixes used for the isothermal calorimetry tests did not have the micro or macro fibers. Four samples were tested for each of Mix I_m and Mix II_m at 20 °C, whereas three samples were tested for each mix at 10 °C and 5 °C. Immediately after mixing, about 10 g of the sample was placed into a 20 mL glass ampoule and kept in the calorimeter, along with a reference sample of water in another ampoule, which acted as an inert sample to improve the signal to noise ratio and identify the temperature artefacts and fluctuations. More detailed information regarding the procedure can be found in [14,69].

2.3. Degree of hydration from ^{29}Si MAS NMR

The development of cement hydration were investigated in both mixes at three different curing temperatures; 20 °C, 10 °C and 5 °C using ^{29}Si MAS NMR (solid-state Magic-Angle Spinning Nuclear Magnetic Resonance), which provides information about the degree of hydration for alite and belite and the fraction of silica fume consumed in pozzolanic reactions. Three master samples of each mix were made and cured separately at the respective temperatures. Similar to that in the isothermal calorimetry tests, the mixes used for the ^{29}Si NMR experiments did not have the micro or macro fibers. On the desired age of hydration, a small slice of the master sample was cut and ground into very fine powder. Isopropanol was then added to the powder to stop the hydration in the sample. The sample was kept in isopropanol for 3 days, after which it was filtered out and stored in a vacuum desiccator until the day of testing. More details regarding the specimen preparation could be found in Chapter 1 of [70].

The ^{29}Si MAS NMR spectra were recorded at 59.6 MHz on a Varian-INOVA 300 MHz (7.05 T) spectrometer, using a home-built CP/MAS probe for 5 mm outer diameter (o.d.) partially sintered zirconia (PSZ) or Si_3N_4 rotors (130 µl sample volume) and a spinning speed of 10.0 kHz. Single-pulse excitation with a 2.5 µs pulse width (~45° flip angle) for a radio frequency field strength of $\gamma B_1/2\pi \approx 50.0$ kHz was employed along with a 30 s repetition delay and typically around 8.000–12.000 scans. The rather high spinning speed of 10.0 kHz was chosen, as no spinning sidebands occur under these conditions in the NMR spectra, which improves the precision of the deconvolution analysis. Furthermore, the relaxation delay of 30 s corresponds to full relaxation under the present conditions, as judged from an array of spectra obtained with different relaxation delays. Neat tetramethyl silane (TMS) was used as the ^{29}Si chemical shift reference, employing larnite (β-Ca_2SiO_4, $\delta = -71.33$ ppm) as a secondary standard.

The deconvolutions of the ^{29}Si NMR spectra were performed with the Varian VnmrJ software, using procedures described elsewhere for anhydrous [71,72] and hydrated Portland cements [73,74]. This approach gives relative intensities for ^{29}Si in alite, belite, silica fume and the for Q^1, Q^2, and $Q^2(1Al)$ resonances of the C-(A-)S-H phase. The degrees of hydration (H) for the anhydrous phases were calculated as described in Section 3.2.

Table 4
Properties of Mix I and II in the fresh state (average value from 4 tests).

Property	Units	Mix I	Mix II
Workability (ASTM - spread after 25 blows)	mm	179	146
Specific weight	kg/m^3	2834	2695
Air content	%	3.2	4.7

2.4. Dynamic and static modulus of elasticity

The dynamic modulus of elasticity was determined on cylinders of dimensions 140 mm × 70 mm, using Vibration Resonance Frequency Tests (VRFT) [14,75], right after the setting of the specimens. A steel ball of 1 cm was made to hit the center of one of the circular faces of the cylinders, which produced longitudinal vibrations in the specimen. The vibrations were captured by a miniature accelerometer attached in the center of the circular face at the other end of the cylinder. Using a LABVIEW program, the measured signal was converted into a FFT

Table 3
Properties of Mix I and II in the hardened state, cured at 20 °C.

Property	Units	Mix I	Mix II	Age (days)
Tensile first crack strength, f_{Ute}* (average of 8 tests)	MPa	12.3 ± 1.7	11.1 ± 1.9	14
Uniaxial tensile strength, f_{Utu} (average of 8 tests)	MPa	18.0 ± 3.1	15.1 ± 2.7	14
Modulus of elasticity in tension (average of 8 tests)	GPa	51.0 ± 2.3	46.3 ± 1.3	14
End of tensile hardening (average of 10 tests)	‰	1.64 ± 0.44	1.27 ± 0.51	14
Compressive strength (average of 3 tests)	MPa	230.5 ± 0.85	169.7 ± 0.5	28
Modulus of elasticity in compression (average of 3 tests)	GPa	48.3 ± 0.8	46.3 ± 0.8	28
Sorptivity (average of 10 tests)	gr/m$^2\sqrt{h}$	45.0 ± 5.2	32.5 ± 9.5	28

* Corresponds to the transition from the elastic behavior to the strain hardening behavior.

Table 5
Summary of uniaxial tensile tests to determine the resistance parameters like f_{Ute} and f_{Utu}.

Age (days)	Mixes	Temperature	Test setup
1	Mix I	20 °C	TSTM
	Mix II	20 °C	TSTM
14	Mix I	20 °C, 5 °C	KAPPA 250 DS
	Mix II	20 °C, 10 °C, 5 °C	KAPPA 250 DS
30	Mix I	20 °C, 5 °C	TSTM
	Mix II	20 °C, 10 °C, 5 °C	TSTM
80	Mix I	20 °C	TSTM

domain to obtain the first two resonance frequencies in the frequency spectrum. Using an analytical procedure as mentioned in [75], the dynamic elastic modulus of the specimens were calculated. The tests were carried out in a climate chamber where the samples were cured under three different temperatures; 20 °C, 10 °C and 5 °C, for both mixes. The measurements were started from the setting time until one month or more, at a frequency of one measurement per minute. Even though the measured elastic modulus was the elastic modulus in compression, it was assumed to be the same as elastic modulus in tension.

The static modulus of elasticity was determined on cylindrical samples of 140 mm height and 70 mm diameter, following SIA 262/1 – Annex G [76]. The tests were carried out on samples cured at three different temperatures; 20 °C, 10 °C and 5 °C, right after casting until the day of testing.

2.5. Uniaxial tensile tests

Uniaxial tensile tests until fracture were carried out on specimens of both mixes to investigate the tensile resistance parameters like elastic limit, f_{Ute} and tensile strength f_{Utu} under different curing temperatures. The tests were performed at different ages as summarized in Table 5. The tests at 1 day and 28 days were carried out on specimens cast directly in the RS setup of the TSTM (cross section 100 mm × 50 mm) at a stroke rate of 0.2 mm/min, whereas the tests at 14 days were conducted on dumbbell specimens of dimensions 50 mm × 30 mm in an electromechanical test setup KAPPA 250 DS from ZWICK/ROELL at a strain rate of 1×10^{-5} 1/s. More details regarding the electromechanical test setup and specimen preparation can be found in [11].

2.6. Development of autogenous deformations

A Temperature Stress Testing Machine (TSTM) was used to measure the autogenous deformations in the mixes right after casting, at different curing temperatures. Fig. 1 shows the schematic representation of the TSTM test setup.

The machine which was developed during the doctoral thesis of [18], following the works of [77–79], consists of two parts; the Free Setup (FS), which was used to measure the free autogenous deformations $\varepsilon_{free}^{free}$ in the specimen, and the Restrained setup (RS), which was used to measure the eigenstresses under different restraint conditions with the help of a load cell. More details on the test setup and measurements could be found in [5,9,21]. The cross sectional dimensions of the specimen used in both setup were 100 mm × 50 mm. The tests were carried out for both mixes at three different temperatures; 20 °C, 10 °C and 5 °C, as summarized in Table 6.

2.7. Development of eigenstresses under full restraint

The RS setup of the TSTM was used to conduct full restraint tests at different quasi-isothermal curing temperatures. The relative displacements between two LVDTs 750 mm apart, were kept at zero in order to ensure the full restraint conditions in the specimen. However, this was not possible in the fresh state, as the material stiffness was too low to impose a close loop deformation control. As such, the tests were started under a passive control by keeping the stroke at the same initial position, until the eigenstresses reached a value of 0.2 MPa. When the trigger value of 0.2 MPa was reached, the control was shifted to deformation control, ensuring full restraint conditions from thereon. The trigger value of 0.2 MPa (corresponding to a force of 100 kg carried by the specimen) was chosen so that it is low enough to minimize the discrepancies of the control mode and the impacts on the viscous effects of the loading history. However, it is still high enough to reach a sufficient stiffness of the specimen to respond to a closed loop deformation control without yielding out of control. The tests were carried out for both mixes at three different temperatures; 20 °C, 10 °C and 5 °C, as summarized in Table 6.

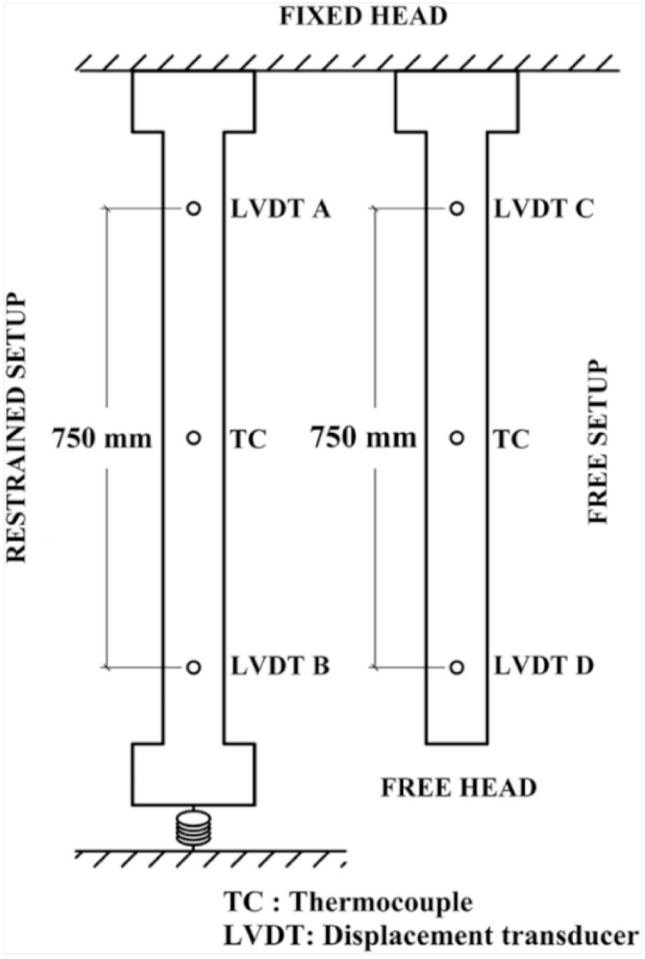

Fig. 1. Schematic representation of the TSTM setup (adapted after [9,18]).

Table 6
Summary of tests carried out in the TSTM.

Mix type	Temperature	Number of tests	Test name
Mix I	20 °C	2	Mix I-20C-FR1
			Mix I-20C-FR2
	5 °C	1	Mix I-5C-FR1
Mix II	20 °C	2	Mix II-20C-FR1
			Mix II-20C-FR2
	10 °C	1	Mix II-10C-FR1
	5 °C	2	Mix II-5C-FR1
			Mix II-5C-FR2

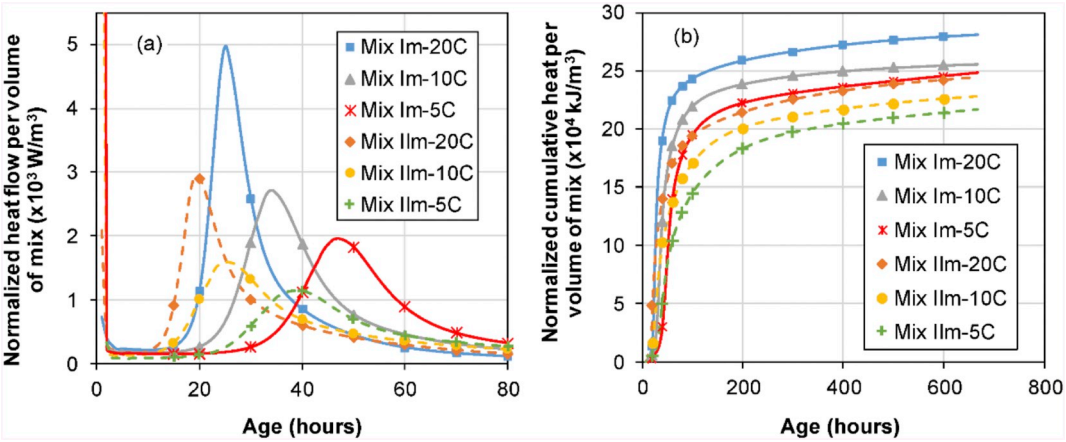

Fig. 2. (a) Average cumulative heat per unit volume and (b) average heat flow per unit volume of Mix I_m and II_m from isothermal calorimetry tests at different temperatures.

3. Results and discussions

3.1. Isothermal calorimetry

3.1.1. Heat of hydration

Fig. 2a shows the average normalized heat flow per volume of the mixes Mix I_m and Mix II_m and Fig. 2b shows the normalized cumulative heat per volume of the same. Only the average curves are shown as the scatter between different tests at each temperature were < 0.01%. The normalization was performed by calculating the volume of 10 g of paste that was put in the ampoule using the specific weight of both mixes (2295.9 kg/m^3 for Mix I_m and 2199.6 kg/m^3 for Mix II_m).

Comparing the two mixes, Fig. 2a shows that Mix II_m exhibited a lower dormant period than Mix I_m, at similar temperatures. This could be attributed to the difference in the dosages of the superplasticizer used in the mixes to reach the minimum workability, with Mix I_m having a superplasticizer content of 20.5 kg/m^3 and Mix II_m having the same at 14.7 kg/m^3. However, it could also reflect a greater nucleation of C-S-H on the surfaces of the limestone filler in Mix II_m. Berodier and Scrivener [80] showed that C-S-H nucleate preferentially on the limestone surface and the amount of C-S-H nuclei formed on the limestone filler surface was much higher than that on the surface of the cement grains. They also postulated that the lower induction period might be caused by the slight dissolution of limestone, which was indicated by a higher concentration of calcium in the solution at the end of the induction period. Moreover, using TEM images, Bazzoni [81] showed a different morphology of C-S-H nuclei on the surfaces. The C-S-H were in the form of individual needles perpendicular to the surface on the limestone grains, whereas the orientation was much different on the cement grains. This also indicated that the C-S-H nucleate preferentially on the surfaces of the limestone filler. Furthermore, Fig. 2a also shows that a higher curing temperature results in a higher heat flow rate, a lower induction period and a narrower hydration peak in the isothermal calorimetry curves. Similar trends were also reported in [82–86]. The higher peak and lower induction period at higher temperature result from the higher rate of hydration, whereas at lower temperatures, the rate of hydration is slower and gradual. This also leads to the development of better microstructure with fewer and lesser number of pores at low temperatures [37].

Comparing the same mix at different temperatures in Fig. 2, it can be seen that both the heat flow and the cumulative heat is higher at a temperature of 20 °C than those at 10 °C and 5 °C. This could be attributed to the faster rate of hydration at higher temperatures. However, many authors reported that the cumulative heat of hydration at lower temperatures become higher than that at higher temperatures at later ages of hydration [38,39,83,85], owing to higher degree of hydration at later ages for lower temperatures. Even though this trend was not seen until 650 h in the present study, it was seen that the difference between the cumulative heats of hydration for both mixes was reduced at later ages especially for tests at 10 °C and 5 °C. Similar trends were seen by Kazemi Kamyab [14] for UHPC mixes similar to those in the present study, who attributed this difference to the presence of silica fume in the mixes as compared to that of [38,39]. However, Gallucci et al. [37] showed that the degree of hydration at 1 year remains the same for cement pastes tested at different temperatures varying from 5 °C to 60 °C, thereby indicating that the cumulative heat of hydration may also become similar at a later age. Fig. 2b also shows a lesser cumulative heat of hydration for Mix II_m when compared to Mix I_m at any temperature. It seems that compared to Mix I_m, slightly lesser volumes of cement are hydrating in Mix II_m (same for silica fume). This may be because of the very dense nucleation of C-S-H in the presence of limestone filler, as discussed earlier, which prevents the water from reaching the unhydrated cement grains, as the microstructure develop. However, further studies using SEM micrographs are needed to validate this argument.

3.1.2. Maturity and activation energy

Different methods could be used to find the activation energy of cumulative heat of hydration from isothermal calorimetry tests as can be found in [14,87–89]. In this study, the master curve method using the maturity Eq. (1) as reported in [14] was used to determine the apparent activation energy, E_a, corresponding to the development of the cumulative heat of hydration from the isothermal calorimetry tests for both mixes. The apparent activation energy (E_a) in Eq. (2) was changed until the cumulative heat of hydration curves at different temperatures converged in the maturity domain. The cumulative heat of hydration curves in the age domain as well as in the maturity domain are shown in Fig. 3.

$$M(t) = \int_0^t e^{\frac{E_a}{R}\cdot\left(\frac{1}{273+T_{ref}} - \frac{1}{273+T(t)}\right)} dt \quad (1)$$

where M(t) is the maturity function in hours, E_a is the apparent activation energy in J/mol, R is the ideal gas constant = 8.314 J/(mol·K), T_{ref} = 20 °C is the reference temperature and T(t) is the development of temperature in the specimen in centigrade. In an isothermal case, Eq. (1) simplifies into a scalar multiplied by time as shown in Eq. (2),

$$M(t) = t.\ e^{\frac{E_a}{R}\cdot\left(\frac{1}{273+T_{ref}} - \frac{1}{273+T(t)}\right)} \quad (2)$$

Using a least-squares regression analysis, the E_a/R values for Mix I_m and Mix II_m were found to be 3300 K and 4000 K, respectively. The E_a/R for Mix I_m was the same as that reported by [14], who had conducted

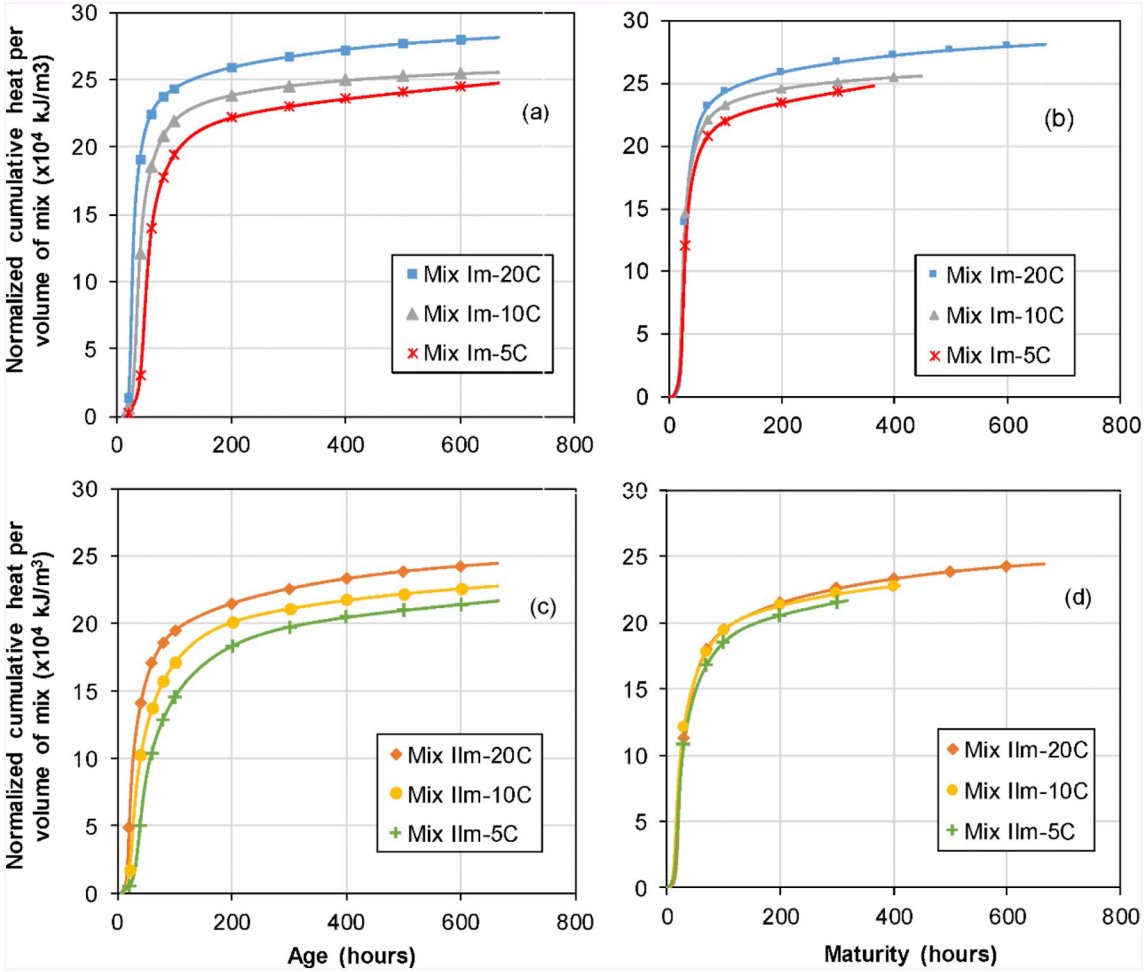

Fig. 3. Average cumulative heat per unit volume of Mix I_m in the (a) age domain (b) maturity domain and for Mix II_m in the (c) age domain and (d) maturity domain.

isothermal calorimetry tests on a similar UHPC matrix of type CM22_TKK, which is the predecessor of Mix I in the present study. Fig. 3 shows that the cumulative heat of hydration curves at different temperatures converge in the maturity domain into nearly one curve, except for the slight variations in the values of cumulative heat of hydration of Mix I_m at a later maturity.

3.1.3. Double Danish model

Even though the conventional 'Danish model' introduced by Hansen and Pedersen [90] predicts the development of cumulative heat of hydration for conventional cementitious materials, [14] showed that it cannot predict the behavior of mixes with extensive amounts of silica fume and supplementary cementitious materials. As such, a 'Double Danish model', as suggested by [91], was used to predict the behavior of the present UHPC mixes. It was assumed that the main heat release from the formation of C-S-H during the hydration of cement was represented by the first term and the remaining heat release associated with the pozzolanic reaction of silica fume was covered by the second term. The double Danish model is given in Eq. (3).

$$H_T(t) = H_{T_1}.\, e^{-\left(\frac{\tau_1}{t}\right)^{\beta_1}} + H_{T_2}.\, e^{-\left(\frac{\tau_2}{t}\right)^{\beta_2}} \quad (3)$$

$$H_{T_\infty} = H_{T_1} + H_{T_2} \quad (4)$$

Here, $H_T(t)$ is the development of cumulative heat of hydration in kJ/m^3, H_{T1} and H_{T2} are the primary and secondary contributions respectively to the heat of hydration, τ_1 and τ_2 are the hydration time parameters of the first and second terms of the double Danish model in hours, β_1 and β_2 are the hydration slope parameters of the first and second terms of the model, and $H_{T\infty}$ is the asymptotic value of the cumulative heat of hydration of the mixes.

Instead of developing multiple models for different temperatures, a representative cumulative heat of hydration curve was developed for each mix as shown in Fig. 4. Using a least-squares regression analysis, the parameters of the double Danish model were determined for both mixes, such that the responses of the representative cumulative heat of hydration curves were closely predicted. Fig. 4 shows the representative curves along with their predictions for both mixes. The parameters of the model for both mixes are shown in Table 7.

3.1.4. Degree of hydration

The degree of hydration at any time, α(t), can be estimated by dividing the cumulative heat of hydration per unit volume of the mixes $H_T(t)$ by the theoretical total potential heat of hydration that would have been released if there was full hydration, $H_{T100\%}$, as shown in Eq. (5) [38].

$$\alpha(t) = \frac{H_T(t)}{H_{T_{100\%}}} \quad (5)$$

The theoretical total heat released can be obtained by considering the individual contributions of total heat of hydration for full hydration of both cement and silica fume in the mixes, as the contributions of the other components are negligible. Moreover, [14,92] have shown that only a maximum of 20% mass of silica fume (SF/C = 0.2) contributed to the heat of hydration, as all the $Ca(OH)_2$ produced by cement hydration will be consumed by then and there will be no more pozzolanic reaction. Table 8 shows the total potential release of both mixes at full

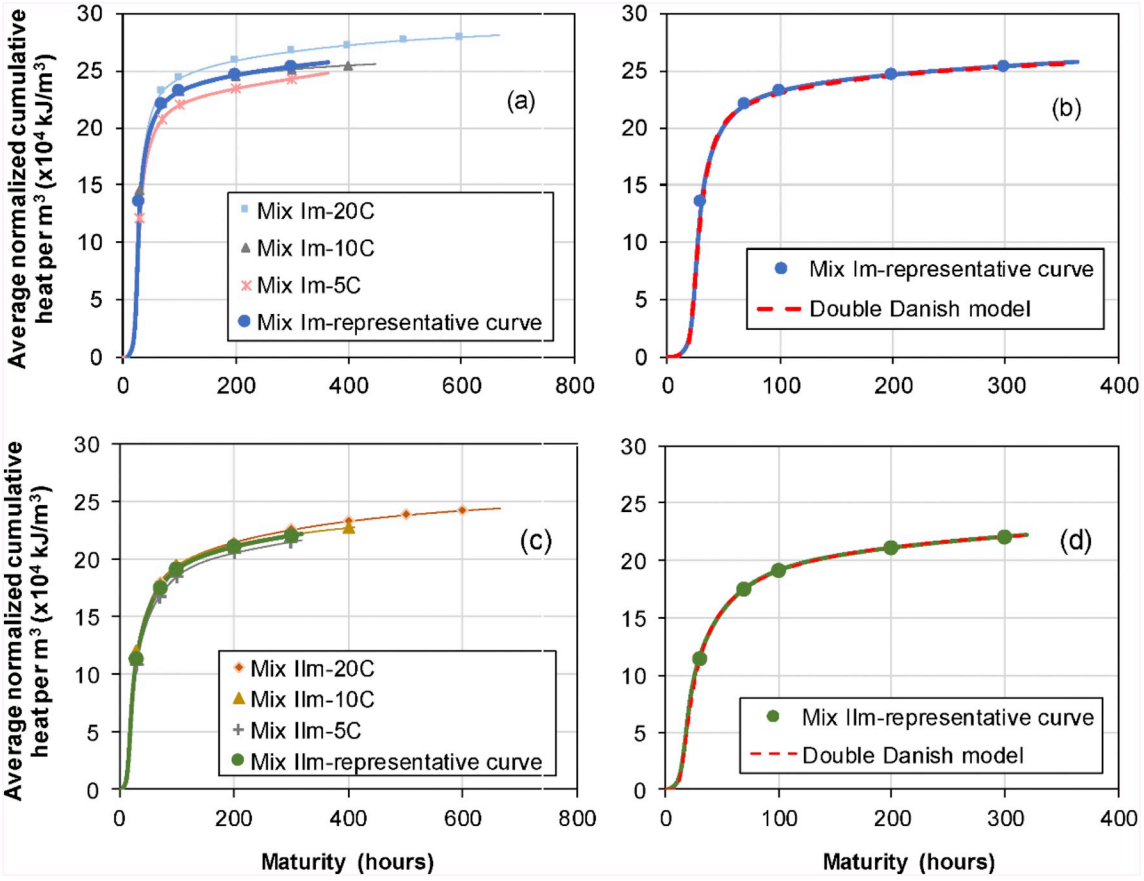

Fig. 4. (a) Representative cumulative heat per unit volume of Mix I_m, (b) Double Danish model prediction of Mix I_m, (c) representative cumulative heat per unit volume of Mix II_m, and (d) Double Danish model prediction of Mix II_m.

Table 7
Parameters of the double Danish model for Mix I and II.

Activation energy	Parameter	Units	Mix I_m	Mix II_m
	E_a/R	K	3300	4000
Double Danish model parameters	H_{T1}	kJ/m^3	192,000	144,000
	τ_1	hours	25.3	20.0
	β_1	–	3.99	2.28
	H_{T2}	kJ/m^3	95,000	105,000
	τ_2	hours	81.2	69.0
	β_2	–	0.64	0.77
	HT_∞	kJ/m^3	287,000	249,000

hydration.

The degree of hydration at any age for both mixes can be obtained by eq. (5). Fig. 5 shows the development of degree of hydration with respect to the age and maturity of the material at different temperatures. Using the ultimate heat of hydration, HT_∞ from Table 7 and Eq. (5), the ultimate degrees of hydration of Mix I_m and Mix II_m were calculated to be 29% and 51%, respectively. The maturity as well as the degree of hydration can be used as domains alternative to the age of the material and the responses under different temperatures could be compared for various mechanical properties in these domains as discussed in the upcoming sections.

3.2. Degree of hydration from ^{29}Si MAS NMR

Fig. 6 shows typical ^{29}Si MAS NMR spectra of the hydrated samples (Mix I_m cured at 20 °C) and each spectrum has been analyzed in a semi-quantitative manner, using the same procedures for spectral deconvolution of ^{29}Si MAS NMR spectra, as described in [71–74]. The analysis of the ^{29}Si NMR spectrum of the anhydrous Portland cement gives an alite/belite intensity ratio of 10.9 (molar ratio), and combining this ratio with the bulk SiO_2 content of the cement (22.75 wt%) gives quantities of 5.5 wt% Ca_2SiO_4 and 79.2 wt% Ca_3SiO_5, assuming stoichiometric phases. If the Taylor compositions are used [71,72], which consider the most common guest-ion incorporations, the calculated quantities for belite and alite are 6.6 wt% and 83.1 wt%, respectively.

The relative ^{29}Si NMR intensities (I) and degrees of hydration (H) for alite and belite and the percentage of silica fume reacted (α_{SF}) from the deconvolutions of the ^{29}Si MAS NMR spectra of Mix I_m and Mix II_m respectively, at different temperatures are shown in the Appendix A,

Table 8
Total potential heat release of Mix I_m and Mix II_m at full hydration, $H_{T100\%}$.

Mix	Cement reacted (kg/m^3)	Heat release of cement for full hydration (kJ/kg) [18]	Silica fume reacted (kg/m^3)	Heat release of silica fume for full hydration (kJ/kg) [92]	Total potential heat at full hydration, $H_{T100\%}$ (kJ/m^3)
Mix I_m	1616.2	452.3	323.2	780	983,134
Mix II_m	809.6	452.3	161.9	780	492,480

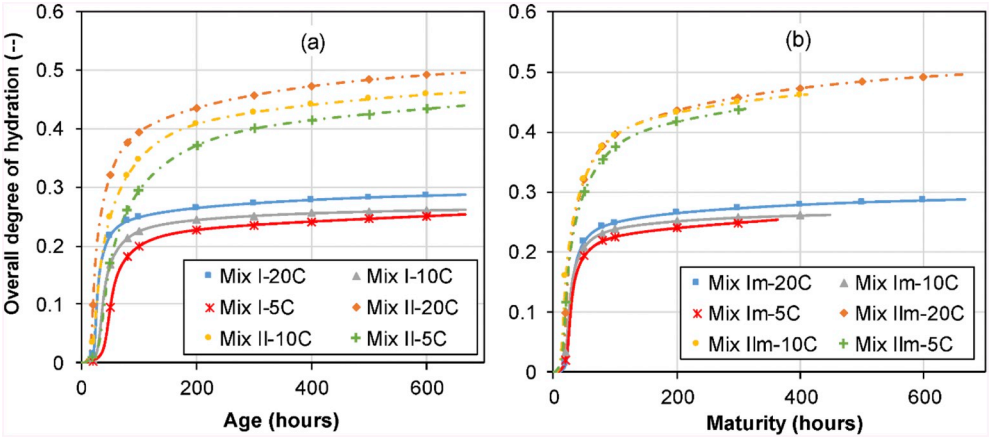

Fig. 5. Development of overall degree of hydration of Mix I_m and Mix II_m at different temperatures, calculated using Eq. (5), from the cumulative heat of hydration curves from isothermal calorimetry tests in the (a) age domain and (b) maturity domain.

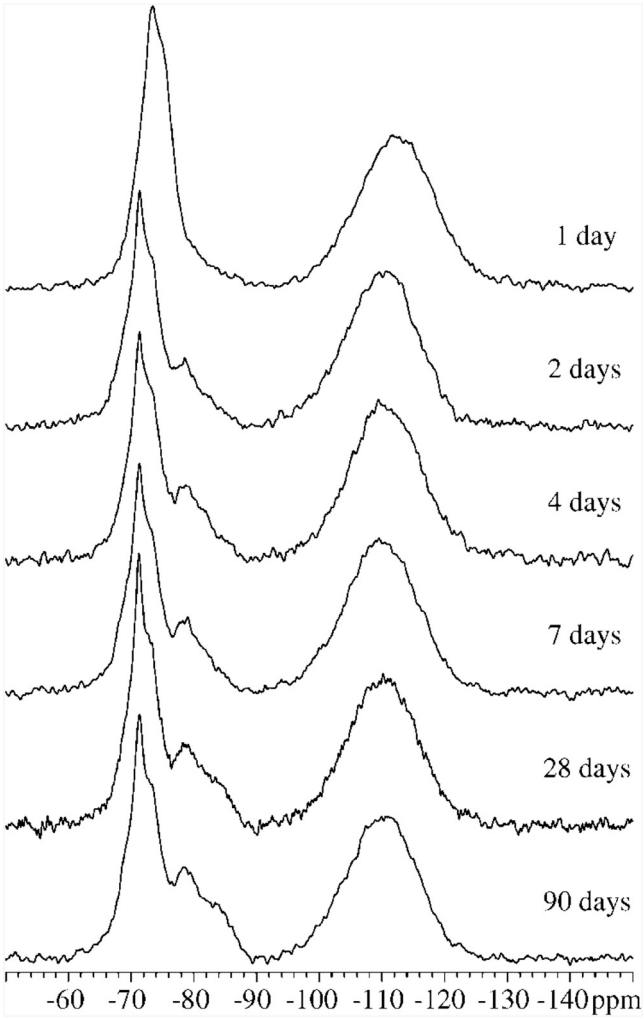

Fig. 6. ^{29}Si MAS NMR spectra of the hydrated samples of Mix I_m cured at a temperature of 20 °C.

Tables A1 and A2. The error limits associated with the degrees of hydration for alite, belite and silica fume are estimated to ± 1.5%, ± 4.0% and ± 1.2%, respectively. The higher error limit for belite reflects the low intensity of the belite peak and as such, a small change may lead to a higher effect on the degree of reaction. The degrees of hydration of alite and belite and the percentage of silica fume reacted are given by Eqs. (6), (7) and (8), respectively. The overall degree of hydration of the cement including the contributions of alite and belite is calculated using eq. (9), where 0.055 and 0.792 are fractions of alite and belite determined from the analysis of the ^{29}Si NMR spectrum of the anhydrous Portland cement.

$$H_{C_2S} = \left(1 - \frac{I(C_2S)_t}{I(C_2S)_{t=0}}\right).100\% \quad (6)$$

$$H_{C_3S} = \left(1 - \frac{I(C_3S)_t}{I(C_3S)_{t=0}}\right).100\% \quad (7)$$

$$\alpha_{SF} = \left(1 - \frac{I(SF)_t}{I(SF)_{t=0}}\right).100\% \quad (8)$$

$$\alpha_{cem} = H_{C_2S}.\frac{0.055}{0.055 + 0.792} + H_{C_3S}.\frac{0.792}{0.055 + 0.792} \quad (9)$$

Fig. 7 shows the development of the degree of cement hydration, α_{cem}, calculated using Eq. (9) for both mixes in the age domain along with a comparison of that of the matrix of CM22_TKK (CM22_TKK$_m$) which is the predecessor of Mix I in the present study. The α_{cem} of Mix I_m at 20 °C was almost similar to that of CM22_TKK$_m$ until an age of 28 days, but shows a deviation at 90 days with Mix I_m showing a α_{cem} of 0.23 while CM22_TKK$_m$ shows a value of 0.33.

This significant difference may reflect differences in the sample preparations or errors associated with the test measurements. Moreover, both the Waller model [92] and the Jensen model [93] predicted a value of 0.30 as the ultimate α_{cem} of Mix I_m. Mix II_m shows a much higher value of 0.47 at 90 days, whereas the predictions of Waller model and Jensen model were respectively 0.47 and 0.5. For both mixes, the influence of thermal activation of hydration is evident, with higher curing temperature leading to a higher α_{cem} at any particular age, except for Mix I_m at 10 °C at an age of 7 days (168 h) and 28 days (672 h). Even though earlier research [38,44] have shown that lower curing temperature may lead to a higher degree of hydration at later ages, it still does not fully explain why at 7 days and 28 days, the α_{cem} of Mix I_m cured at 5 °C was almost similar to that at 20 °C, but that in the case of 10 °C, it was much lower. For Mix II_m, the influence of thermal activation is clear, with α_{cem} at any age decreasing with the decrease in temperature. However, it is possible that at a much later age, α_{cem} becomes the same [37] or even higher for lower temperatures [38,44]. Fig. 8 shows the percentage of silica fume reacted (α_{SF}) as a function of age. The only clear trend is the thermal activation of the pozzolanic reaction, which leads to a higher α_{SF} at any particular age at higher temperatures. Fig. 9 shows the development of α_{cem} in a maturity domain, which shows almost a similar trend as seen in the case of

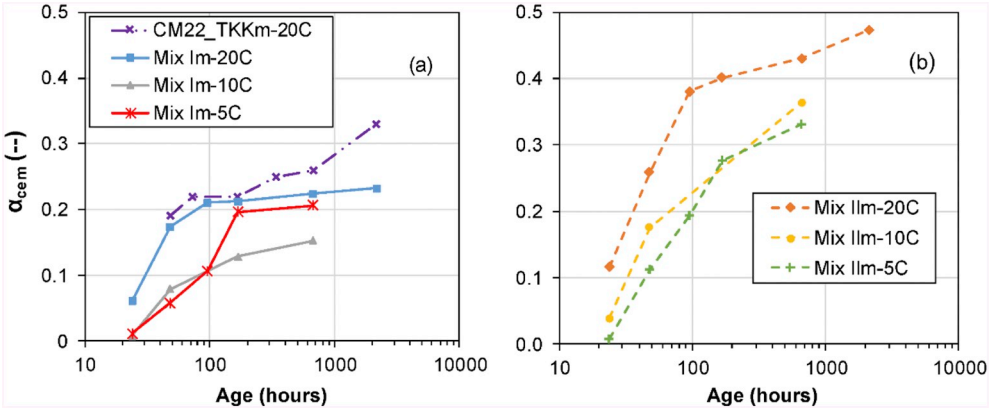

Fig. 7. Development of the degree of cement hydration (α_{cem}) at different temperatures in the age domain for (a) Mix I_m and (b) Mix II_m.

the age domain.

However, a comparison of α_{cem}, α_{SF} and the ratio α_{SF}/α_{cem} in the maturity domain shows an interesting trend. Even though, individually the development of α_{cem} and α_{SF} does not show any particular trend other than the higher thermal activation at higher temperatures, the development of α_{SF}/α_{cem} along the maturity domain shows an initial decrease followed by an increase. The trend was not shown by Mix I_m at 10 °C, and as explained earlier, it was the same Mix I_m at 10 °C that showed unexplainable lower values of α_{cem} at ages of 7 days and 28 days, leading to a conclusion that there might have been errors either in the measurement or the preparation of these samples. Nevertheless, the observed trend of an initial decrease in the α_{SF}/α_{cem} followed by an increase gives an indication that in the beginning, even though there is a limited reaction of the silica fume, the major contribution to the overall degree of hydration of the mixes is that from the cement. However, in the second stage there is a more pronounced reaction of the silica fume, leading to an increase in the α_{SF}/α_{cem} ratio. This indicates that the pozzolanic reaction is also taking place in two stages; an initial stage where the rate of pozzolanic reaction is smaller than that of the direct formation of the C-S-H and a second stage where the trend is reversed.

It is also interesting to note the value of average maturity at which the trend of α_{SF}/α_{cem} is changing from a decreasing rate to an increasing rate. For Mix I, this value was approximately 90 h (excluding the Mix I−10C test) whereas for Mix II it was approximately 70 h (note that this is an approximate average value derived from the limited number of points in the test). It is interesting to observe that these values were similar to the hydration time parameters of the second term τ_2 in the double Danish model as shown in Table 7 with Mix I and II having values of 81.2 h and 69.0 h, respectively. This clearly indicates that the additional accelerated pozzolanic reaction in the second stage contributes to the heat release predicted by the second term of the Double Danish model.

According to the Waller model [92], the ultimate values of α_{cem}, α_{SF} and α_{SF}/α_{cem} were respectively 0.3, 0.28 and 0.93 for Mix I and 0.47, 0.29 and 0.62 for Mix II. Fig. 9 reveals that at an age of 90 h, the experimental results show values of 0.23, 0.14 and 0.6 for Mix I, and 0.47, 0.17 and 0.35 for Mix II for the same. The huge difference in the α_{SF}/α_{cem} values were mainly because the values of α_{SF} were considerably lower than the Waller predictions, but they may reach similar values at a much later age. The values of α_{cem} was lower for Mix I, probably due to errors in the specimen preparation, whereas α_{cem} of Mix II was similar to the prediction of the Waller model.

3.3. Development of elastic modulus

The development of the dynamic elastic moduli from the VRF tests, along with the static elastic moduli for both mixes at different temperatures are shown in Fig. 10. For each mix at a particular temperature, two tests were performed using the VRF and since both the curves almost merged together with minimum scatter, the average of the two curves is shown for each mix and temperature in Fig. 10. For each mix at different temperatures, the dynamic elastic moduli are higher than the corresponding static moduli, as expected. Moreover, the static elastic moduli showed almost similar values at temperatures of 10 °C and 5 °C, which were slightly lesser than those at 20 °C for both mixes. It may be possible that at a much later age, the values of the static moduli become similar under all the temperatures, just as in the case of

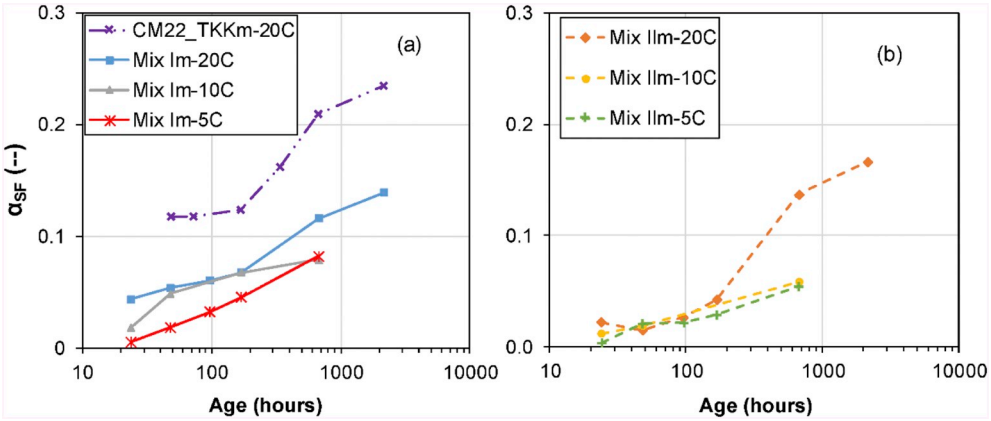

Fig. 8. Development of degree of silica fume reaction (α_{SF}) at different temperatures in the age domain for (a) Mix I_m and (b) Mix II_m.

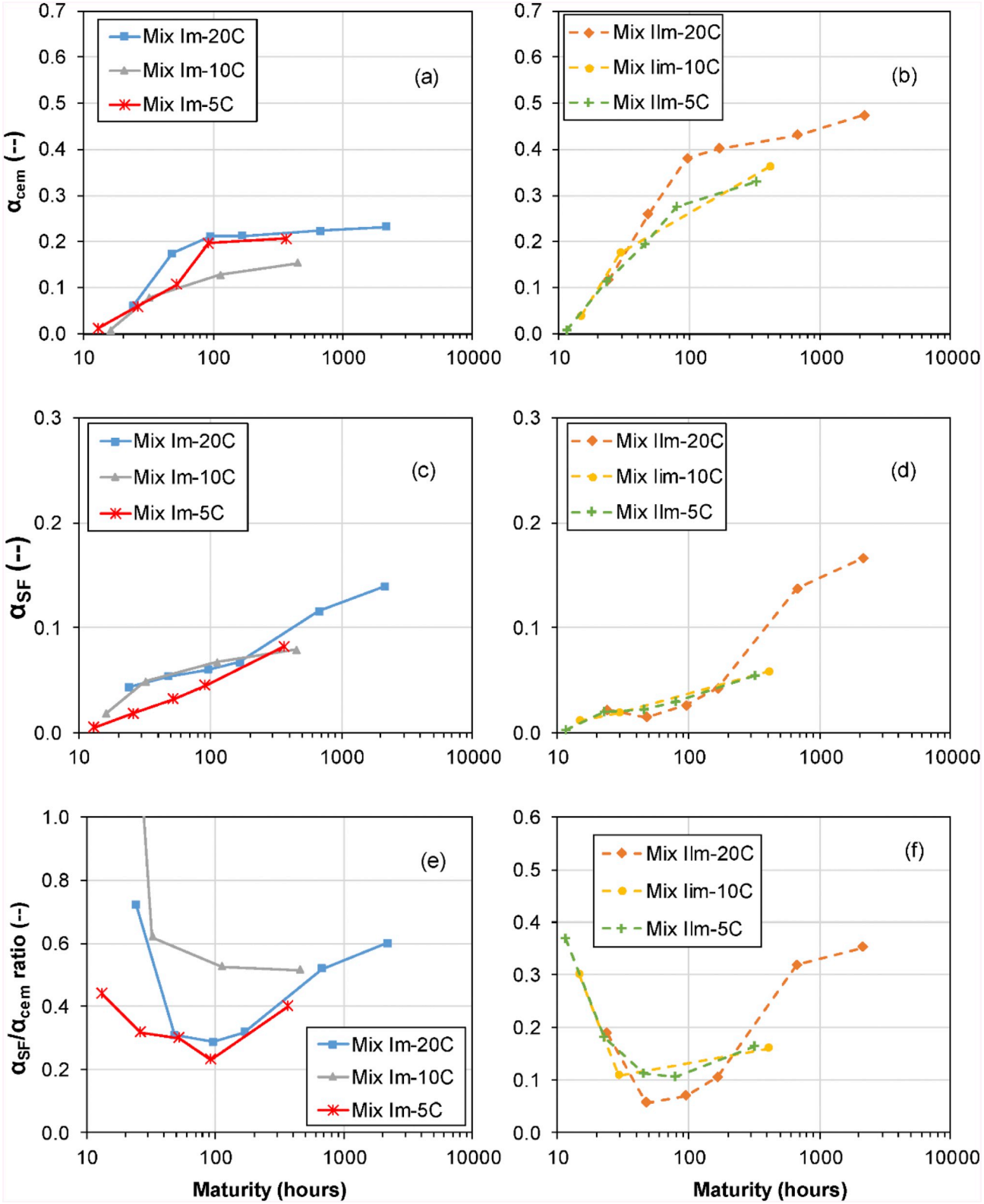

Fig. 9. Development of α_{cem} in the maturity domain for (a) Mix I_m and (b) Mix II_m. Development of α_{SF} in the maturity domain for (c) Mix I_m and (d) Mix II_m. Variation in the α_{SF}/α_{cem} ratio in the maturity domain for (e) Mix I_m and (f) Mix II_m.

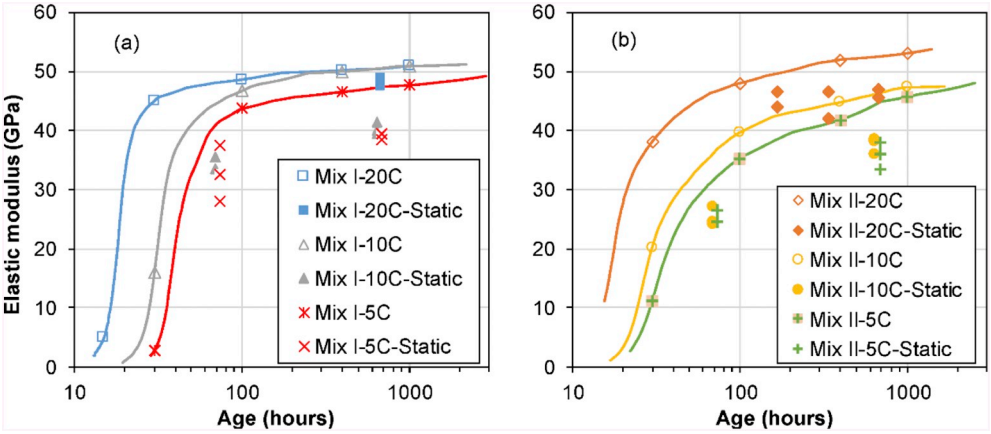

Fig. 10. Development of dynamic and static elastic moduli at different temperatures in the age domain for (a) Mix I and (b) Mix II.

the dynamic elastic moduli as discussed below.

For the dynamic elastic moduli, the development started earlier for 20 °C because of the thermal activation of hydration as in the case of the isothermal calorimetry tests. However, the trend of development of the dynamic moduli at all temperatures is such that the ultimate dynamic elastic moduli reach a similar value of slightly > 50 GPa. There is a contrast in literature regarding the degree of hydration and the corresponding development of mechanical properties at different temperatures for cementitious materials. On the one hand, some studies show that the degree of hydration is higher at a later age for lower temperatures [38,39,44], whereas on the other hand, other investigations show that the ultimate degree of hydration remains the same under different temperatures [37]. In any case, the present study shows a trend to have a similar elastic modulus at a later age, but whether it will be higher for lower temperatures at a much later age cannot be concluded.

Fig. 11 shows the comparison of the dynamic elastic moduli development in Mix I and II at different temperatures. At any particular temperature, the dynamic elastic moduli of Mix I and II are comparable in the beginning, whereas at around an elastic modulus of 20 GPa, the rate of development becomes much slower in Mix II for all the curing temperatures. Moreover, the trend inverts at around an elastic modulus of 40 GPa, and the values for both mixes start converging again. This trend was discussed in detail in the framework of two main parameters; the silica fume/cement (SF/C) ratio and the water/cement (w/c) ratio in [21]. More details can be found in Appendix B.

Following the concepts developed in Sections 3.1.2 and 3.1.4, the development of elastic moduli at different temperatures was studied in

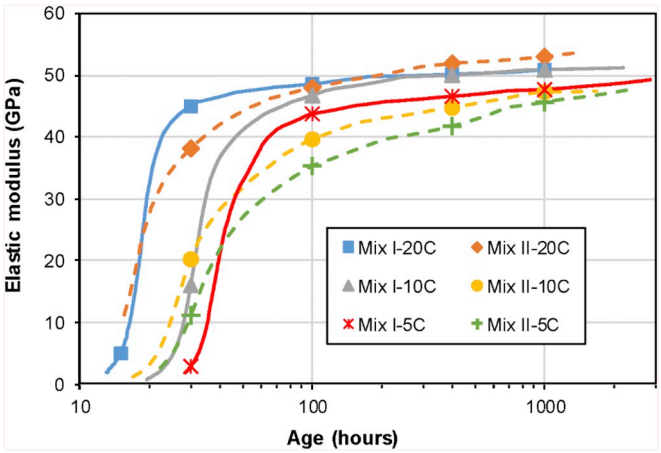

Fig. 11. Comparison of the development of average dynamic elastic modulus of Mix I and II at different curing temperatures in the age domain.

the maturity domain as well as in the degree of hydration domain. Fig. 12 shows the development in the maturity domain whereas Fig. 13 shows the same in the degree of hydration domain. In the maturity domain, a single activation energy (E_a/R = 3300 K for Mix I_m and 4000 K for Mix II_m, Section 3.1.2) can more or less capture the influence of temperature on the development of the elastic modulus except for slight discrepancies for the mixes at 20 °C. In Fig. 12a, the development of elastic modulus for Mix I at 20 °C begins at a slightly earlier maturity, which may be attributed to the relatively higher increase in the temperature in the VRF test cylinders at 20 °C during the hydration of the main components. The maturity axis in Fig. 12 was calculated based on the assumption of isothermal temperature conditions from Section 3.1.2, which is not the case in the VRF samples. Even though this trend is not seen in the Mix II samples in Fig. 12b, the slightly higher values of Mix II at 20 °C at a later age could be attributed either to a better fiber orientation in these mixes or to the fact that the elastic moduli of the other samples at 10 °C and 5 °C may eventually reach these values at a much later age.

The trend is more or less similar in the degree of hydration domain as seen in Fig. 13 with Mix I at 20 °C showing an entirely different trend compared to that of the other cases. This difference may be linked to the calculation of degree of hydration based on the isothermal calorimetry tests where the specimen used is entirely different from that used for the VRF tests. Moreover, the difference could also be attributed to the different mixes used in the tests; mixes with fibers in the VRF tests and mixes without fibers in the isothermal calorimetry tests. Nevertheless, the values of elastic moduli reach almost similar values for Mix I at a degree of hydration of 0.2. The values are similar for Mix II at 10 °C and 5 °C, but shows a slightly higher value at 20 °C for similar degrees of hydration, which could reflect different fiber orientations in the specimens as discussed earlier.

3.4. Tensile resistance from uniaxial tensile tests

Table 9 summarizes the average values of elastic limit, f_{Ute}, and tensile strength, f_{Utu}, at different ages and under different curing temperatures for both mixes. The standard deviation associated with the measurements are also shown, except for certain tests where only one specimen was tested. A decrease can be seen for f_{Ute} and f_{Utu} for certain test series (Mix I-5C-f_{Ute}, Mix I-5C-f_{Utu} and Mix II-10C-f_{Utu}) as the age increases from 336 h (14 days) to 720 h (30 days). This may be because of the smaller cross sectional area of the specimens tested on 14 days (50 mm × 30 mm), which may lead to a more favorable orientation of the fibers when compared to the specimens with a cross sectional area of 100 mm × 50 mm. The trend could also be attributed to the scatter in the test results at different ages. More discussion on the test results is given in section 3.6.

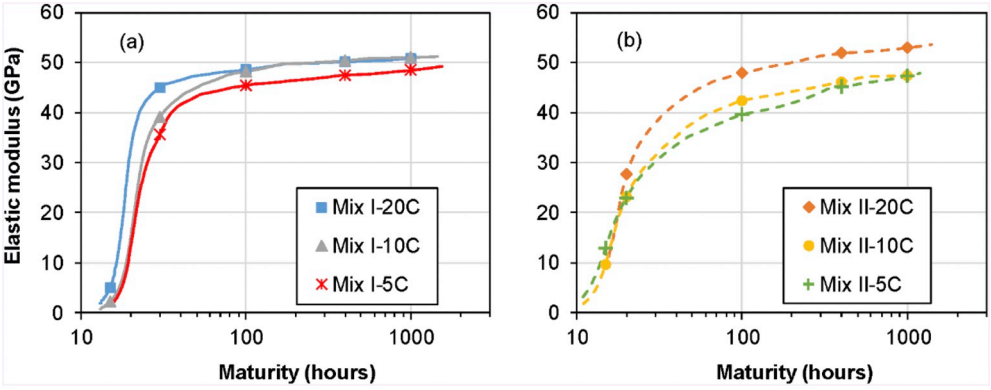

Fig. 12. Development of dynamic elastic moduli at different temperatures in the maturity domain for (a) Mix I and (b) Mix II.

3.5. Development of autogenous deformations

The development of autogenous deformations is shown in Fig. 14, wherein an increasing deformation represents autogenous shrinkage. All the curves have an initial swelling phase in the beginning, as also observed by other researchers for UHPFRC [5,14,55]. However, as indicated in [21], it is the autogenous deformation after the swelling phase that lead to the development of eigenstresses. As such, Fig. 15 shows the development of autogenous deformations zeroed at the end of swelling (autogenous shrinkage). For the ease of comparison, an average response of each mix at a particular curing temperature is shown in Fig. 16.

From Fig. 16, as the curing temperature decreases, the autogenous shrinkage also decreases for both mixes, even though the decrease is much less when the temperature changes from 10 °C to 5 °C for Mix II. Just as in the case of the isothermal calorimetry and elastic modulus, the autogenous shrinkage (after swelling) also starts developing earlier at a temperature of 20 °C, but it is delayed as the temperature decreases. The reduction in the value of the autogenous shrinkage even after an age of 1 month is similar to the trends seen in [7,14,31], while some others have reported non-systematic trends in the development of autogenous shrinkage under different curing temperatures. Kamen et al. [5] showed that the autogenous deformation at 10 °C for a UHPFRC of type CM22, was already higher than the same at 20 °C at an age of 4 days. Lura et al. [35] showed an non-systematic effect of curing temperature on the autogenous shrinkage, but found out that the autogenous shrinkage reached similar asymptotic values at a very later age. Bjontegaard [77] reported an increase in the autogenous shrinkage with both a decrease as well as an increase in the temperature when compared to that at a temperature of 20 °C. Many authors have reported that even though the rate of shrinkage is significantly influenced by the temperature, the magnitude of the shrinkage at a very later age becomes almost similar for all temperatures [29,35].

Table 9
Summary of uniaxial tensile tests.

Mix	Temperature	Age (hours)	Average f_{Ute} (MPa)	Average f_{Utu} (MPa)
Mix I	20 °C	24	8.6 ± 0.3	11.4 ± 0.5
		336	12.3 ± 1.7	15.1 ± 2.3
		720	13.0 ± 1.2	16.2 + 2.0
		1920	13.2	18.1
	5 °C	336	14.2 ± 0.8	19.8 ± 0.9
		720	14.0	16.6
Mix II	20 °C	24	8.1 ± 0.2	9.3 ± 0.2
		336	11.1 ± 1.9	15.1 ± 2.7
		800	13.2 ± 0.5	16.7 ± 0.7
	10 °C	336	12.5 ± 0.6	17.8 ± 1.0
		720	13.2	16.1
	5 °C	336	11.1 ± 0.8	14.8 ± 0.5
		720	12.7 ± 0.8	17.9 ± 1.5

Fig. 17 shows the development of autogenous shrinkage in the maturity domain. It can be seen that the maturity domain does not provide anything additional over the age domain, and therefore does not eliminate the influence of the temperature. This was shown by many researchers previously [14,29,31,35] who attributed this to the dependence of the driving force of the autogenous shrinkage, the capillary stress, on the temperature, as shown by the Kelvin-Laplace equation, Eq. (10). As such, the degree of hydration calculated from the isothermal calorimetry tests were used to compare the autogenous shrinkage developments under different curing temperatures, as shown in Fig. 18.

The comparison between Mix I and II becomes impossible in the degree of hydration domain as both have different ultimate degrees of hydration. Therefore, the results were compared in a degree of reaction

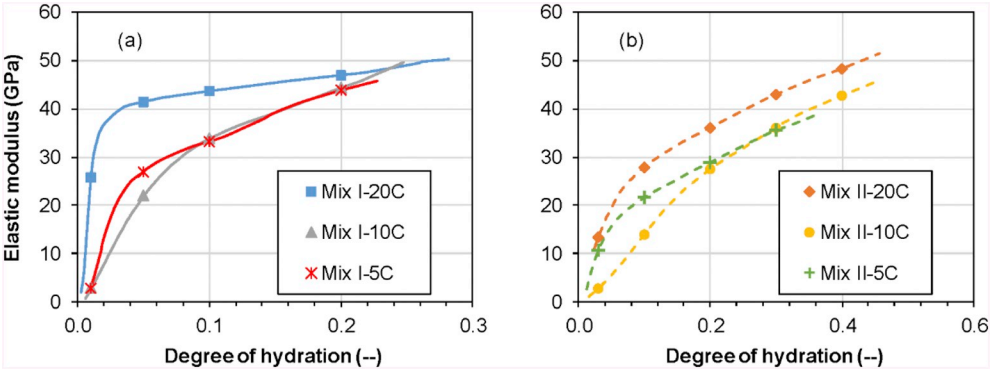

Fig. 13. Development of dynamic and static elastic moduli at different temperatures in the degree of hydration domain for (a) Mix I and (b) Mix II.

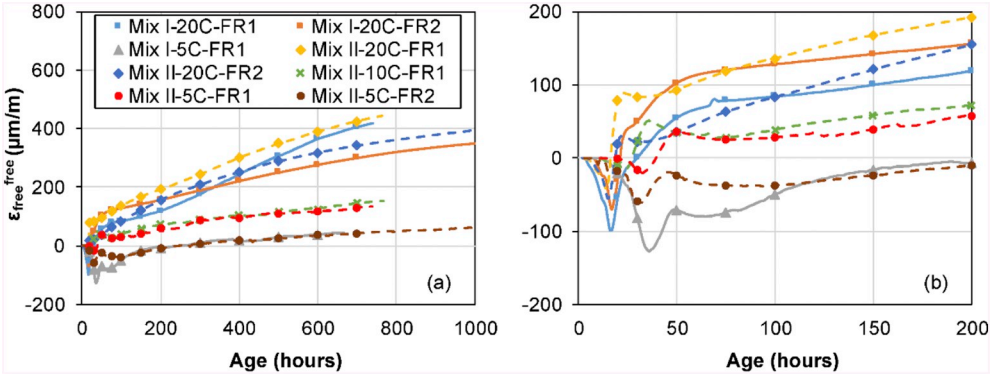

Fig. 14. Development of autogenous deformations as measured (with an initial swelling phase) in the FS setup of TSTM for Mix I and II at different quasi-isothermal temperatures in the age domain; (a) overall behavior and (b) early-age behavior.

(DOR) domain, which is defined as the percentage at any time of the ultimate degree of hydration at any time. While the degree of hydration (α(t) in Eq. (5)) can vary only from 0 to 0.29 for Mix I and 0 to 0.51 for Mix II, the degree of reaction can vary from 0 to 1 for both mixes. For example, a degree of hydration of 0.29 for Mix I is equivalent to a degree of reaction of 1 for the same. Fig. 19 shows the comparison of the autogenous shrinkage development for both mixes in the DOR domain.

The kinetics of development of autogenous shrinkage are similar for both mixes at different temperatures. All the tests show an initial increase in the autogenous shrinkage until a DOR of 0.2–0.3 followed by a plateau or slight decrease until a DOR of about 0.6, after which there is again an increase in the autogenous shrinkage. The difference between the values of the autogenous shrinkage at different temperatures at any degree of reaction is considerably less than the difference at any particular age in the age domain. The slightly higher values of the mixes at 20 °C may reflect scatter in the measurements. Nevertheless, the trend at 20 °C is identical to that in the case of elastic modulus development of Mix I at 20 °C, Fig. 13, which shows higher values when compared to those at 10 °C and 5 °C at similar degrees of hydration.

The reduction in the autogenous deformations at lower temperatures can be explained using the capillary stress that develops within the pore fluid [24]. After setting, the self-desiccation in the cement paste produces a negative pressure in the pore fluid, which leads to a tensile capillary shrinkage induced stress. This capillary stress can be described using the Kelvin-Laplace equation as shown in Eq. (10) [24,94],

$$\sigma_{capillary} = -\frac{2\sigma}{r}\cos\theta = -\frac{RT}{Mv}\ln(h) \quad (10)$$

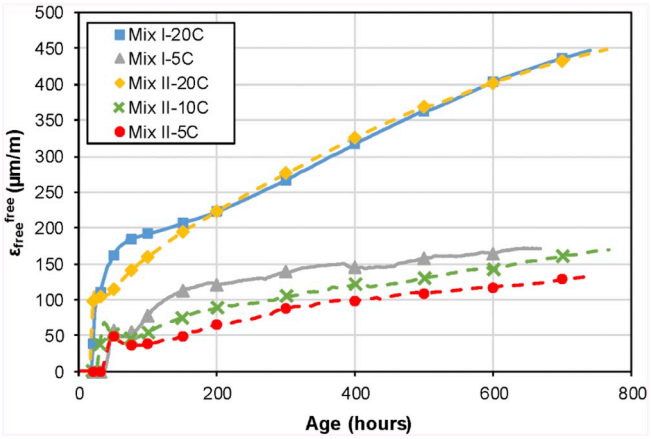

Fig. 16. Comparison of the average autogenous deformations zeroed after swelling at different quasi-isothermal temperatures for Mix I and II in the age domain.

where σ is the surface tension of the water/vapor interface, θ is the moistening angle, r is the radius of the liquid vapor meniscus, Mv is the molar volume of water, R is the ideal gas constant, T is the temperature and h is the relative humidity. Earlier studies [94,95] have shown that when the pore network and the degree of hydration are similar, the main factor that affects the capillary stresses is the change in the surface tension or the internal relative humidity with a change in the temperature. Sant et al. [28] showed that the surface tension of water reduced with an increase in the temperature, which should translate to a

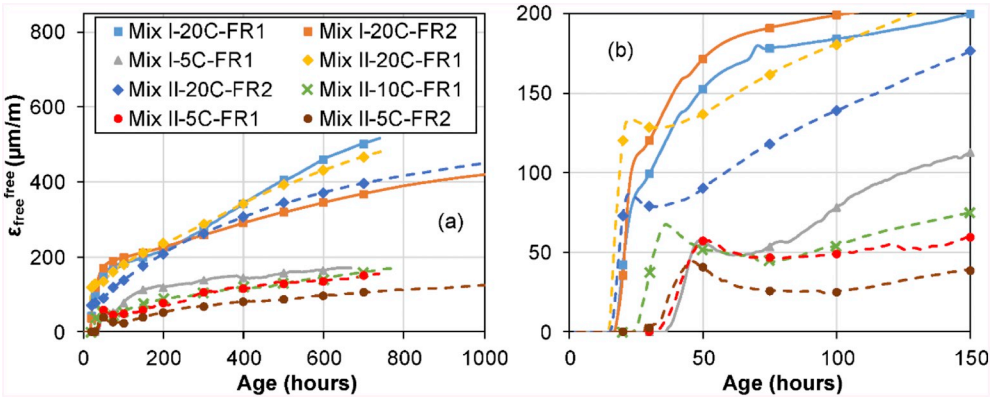

Fig. 15. Development of autogenous deformations zeroed after the swelling for Mix I and II at different quasi-isothermal temperatures in the age domain; (a) overall behavior and (b) early-age behavior.

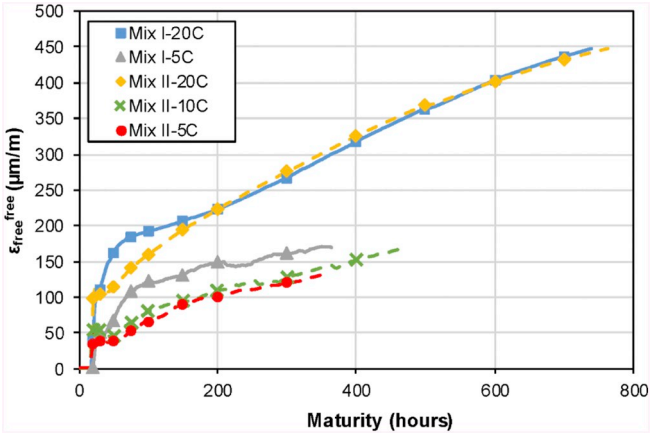

Fig. 17. Comparison of the average autogenous deformations zeroed after swelling at different quasi-isothermal temperatures for Mix I and II in the maturity domain.

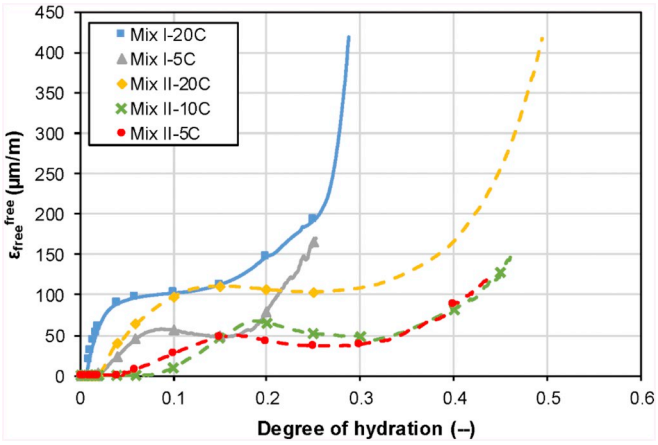

Fig. 18. Comparison of the average autogenous deformations zeroed after swelling at different quasi-isothermal temperatures for Mix I and II in the DOH domain.

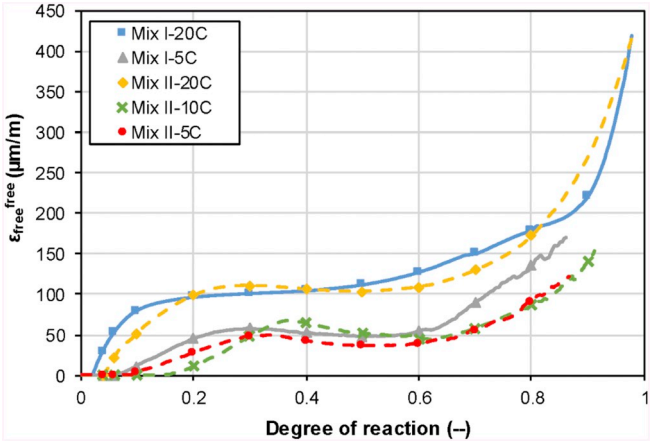

Fig. 19. Comparison of the average autogenous deformations zeroed after swelling at different quasi-isothermal temperatures for Mix I and II in the DOR domain.

corresponding decrease in the capillary stress and thereby the autogenous shrinkage. However, at lower temperatures there is a considerable decrease in the rate of depression of the relative humidity in cement based samples as shown by Jensen and Hansen [31]. As such following Eq. (10), the expected slight increase in the capillary stress because of the increase in the surface tension of the water/vapor interface, is offset by the reduction in the rate of cement hydration at lower temperatures [29]. This leads to a reduction in the rate of autogenous relative humidity decrease, therefore resulting in a higher internal relative humidity on an age scale. Therefore, the capillary stress and the corresponding autogenous shrinkage are reduced at lower temperatures. A similar explanation was also given by [25], who showed that temperature dependency of the surface tension is negligible when compared to the thermal activation of the processes. This also explains the reduced difference in the autogenous deformations in the DOR domain when compared to that in the age or the maturity domain.

3.6. Development of eigenstresses

Fig. 20 shows the development of eigenstresses in the mixes at different temperatures. Except in the case of Mix I at 20 °C, all the other tests showed an initial increase in the stress which was followed by a slight decrease (shoulder effect), and then an increase again. The trend was similar to that in the autogenous shrinkage, as seen in Fig. 15b, wherein all the tests except those of Mix I at 20 °C, showed a similar shoulder effect. Moreover, all tests show a further increase in the rate of development of eigenstresses after the shoulder effect, except for Mix I at 5 °C, which shows a plateau in the stress development around a stress value of 4 MPa. Similar stabilization of the eigenstresses were also found in [14] for a UHPFRC of type CMM22_TKK, which is the predecessor of Mix I in the present study, at temperatures of 5 °C and 1 °C.

The possible explanation of such a phenomenon may be the cancellation of the eigenstresses development due to the autogenous shrinkage by the higher relaxation potential of the mix at a lower temperature of 5 °C, which in turn leads to a stabilization of the stresses. However, there are two contrasting effects of a low curing temperature on the viscous response; on the one hand, a lower temperature leads to a lower creep/relaxation response whereas on the other hand, a lower curing temperature would lead to a lower apparent age (maturity) of the material and consequently a higher viscous response. In the present scenario, it seems that the higher viscous response due to a lower maturity is more dominant than the lower viscous response due to the lower temperature. Another possible explanation, as noted by [29], is that the rate of hydration and consequently the rate of development of capillary stresses (or autogenous deformation) is much slower at lower temperatures in an “age or maturity” scale, thereby leading to more viscoelastic relaxation, when compared to a higher rate of capillary stress at 20 °C. The stress development at lower temperatures is therefore analogous to a test under lower strain rates, thereby leading to higher viscous relaxation. However, a similar stabilization or plateau was not seen in the case of Mix II even at 5 °C, although the viscous potential of Mix II is much higher than that of Mix I, as shown through tensile creep tests in creep rigs in [21]. Nevertheless, it may be possible to see a stress stabilization in Mix II at a later age. Even though the shrinkage strains acting on the mixes were almost similar at 20 °C, the rate of development of eigenstresses were much slower for Mix II. This can be attributed to the higher viscoelastic potential of Mix II, as mentioned earlier, which can lead to a greater relaxation of the developed eigenstresses. The slower development of eigenstresses in Mix II, could also be attributed to the slower rate of development of elastic modulus as seen in Fig. 11. Fig. 21 shows the comparison of average eigenstresses development at different temperatures in an age domain.

Fig. 22 shows the developed eigenstresses under full restraint under various temperatures along with the resistance curves of the elastic limit (f_{Ute}) and tensile strength (f_{Utu}) at these temperatures. The resistance curves were obtained from monotonic tensile tests conducted until fracture for both mixes at different ages. The tests at 1 day (24 h) and after one month (> 720 h) were conducted on the specimens in the TSTM, whereas the tests at 14 days (336 h) were conducted on dumbbell specimens of center cross section 50 mm × 30 mm in an

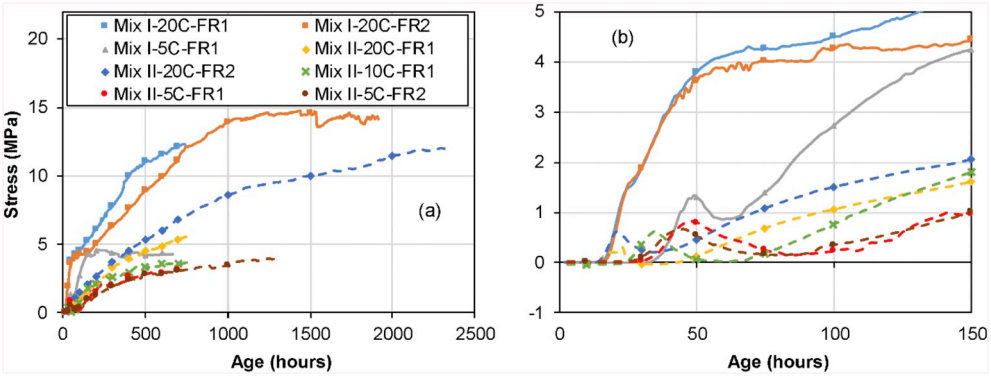

Fig. 20. Development of eigenstresses under full restraint for Mix I and II under different quasi-isothermal temperatures in the age domain; (a) overall behavior and (b) early-age behavior.

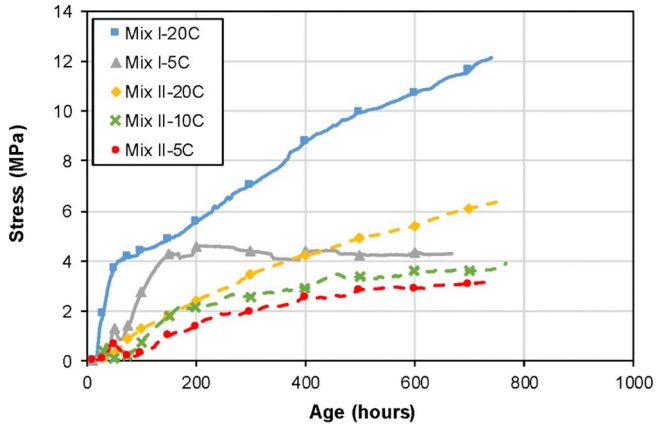

Fig. 21. Comparison of the average eigenstresses development at different quasi-isothermal temperatures for Mix I and II in the age domain.

electromechanical testing machine, KAPPA 250 DS from ZWICK/ROELL with a capacity of 250 kN. The tests at an age of 1 day were conducted only at a temperature of 20 °C for both mixes. More details regarding the uniaxial tests at 14 days can be found in [11].

The cross sectional area of the dumbbell specimens in the uniaxial tests in the ZWICK (50 mm × 30 mm) are smaller than that of the TSTM specimens (100 mm × 50 mm). The orientation of the fibers will be more favorable for the tensile properties in the smaller cross section. This is the reason for a decrease in the resistance curve from 14 days to 30 days as can be seen in the case of Mix I-5C-f_{Ute}, Mix I-5C-f_{Utu} and Mix II-10C-f_{Utu}. Fig. 22 shows that for Mix I-20C-FR2, the eigenstresses reached the strain hardening domain after about 720 h (one month), whereas for Mix II-20C-FR2, the eigenstresses were approaching the strain hardening domain at about 2400 h (just over 3 months). Even for the former, the stresses in the strain hardening domain never reached the tensile strength of the mixes thereby ensuring the absence of a localized macrocrack. This ensures that, if there is no detrimental fiber orientation, both mixes can resist the developed eigenstresses even under fully restrained shrinkage conditions.

Fig. 23 shows the development of the eigenstresses in the maturity domain whereas Fig. 24 shows the same in the DOR domain.

Unlike the autogenous shrinkage, the eigenstresses development is very similar for Mix II in the maturity domain, whereas for Mix I, the trend of stabilization of stresses at 5 °C is not seen in the test at 20 °C. The possible reason for the stabilization was discussed before. In the DOR domain, the eigenstresses development had even lesser scatter than those in the maturity domain. The stress development showed three clear zones; an increase in the beginning followed by a reduced rate of development (Mix I−20C) or a negative rate of development, which was further followed by an increase in the rate of development. Except for Mix I−20C, there was a slight decrease in the stresses from a DOR of about 0.3 to 0.6. This trend was similar to that in the case of the autogenous shrinkage, Fig. 19. Moreover, even in the DOR domain, Mix I showed much higher stresses at a particular value of DOR when compared to Mix II, which could be attributed to the higher relaxation potential of Mix II as discussed before in [21].

4. Material level vs structural level

4.1. Overview

In this section, the trends found in the structural level (autogenous shrinkage and eigenstresses development) will be discussed in view of the trends at a material level (degree of hydration, elastic modulus) in the age domain. For simplification, only the trends at 20 °C are discussed for both mixes. The age domain is divided into three main zones as can be seen in Fig. 25. However, it should be noted that, owing to the difference in the sizes of the specimens used in each test, and also to the type of arrangements for the curing and temperature control, there will be slight changes in the times at which a zone changes to the other. However, the difference is very small as can be seen from the discussions below.

4.2. Zone I

Fig. 25a shows the development of the overall degree of reaction of the mixes, calculated from the isothermal calorimetry tests. In Fig. 5, the development of overall degree of hydration for both mixes, calculated from the cumulative heat released was discussed. However, for comparison of the kinetics of both mixes, the degree of reaction gives a better understanding. In Fig. 25a, the overall degree of reaction of Mix II starts earlier than that of Mix I, due to the earlier setting of Mix II caused by the lower superplasticizer content. However, it becomes similar for both mixes at around 25–30 h, after which the zone II starts. Similar trends were seen in the case of development of elastic modulus, Fig. 25b, and that of autogenous shrinkage, Fig. 25f. It should be noted that in Fig. 25b, zone I is ending around 20 h, slightly lesser than that in the other figures, which could be attributed to the difference in the specimen dimensions and curing conditions as indicated earlier. In Eq. (10), for similar temperatures and pore water, the variables that can be different between Mix I and II are the Kelvin radius r, which depends on the pore structure and the relative humidity, h. Since the elastic modulus is similar for both mixes at the end of zone I, it could be assumed that the microstructure and pore structure, and therefore the pore radius, will also be similar at that point [96]. This would then correspond to a similar capillary stress and therefore similar autogenous shrinkage, which is also experimentally observed in Fig. 25f. At the end of zone I,

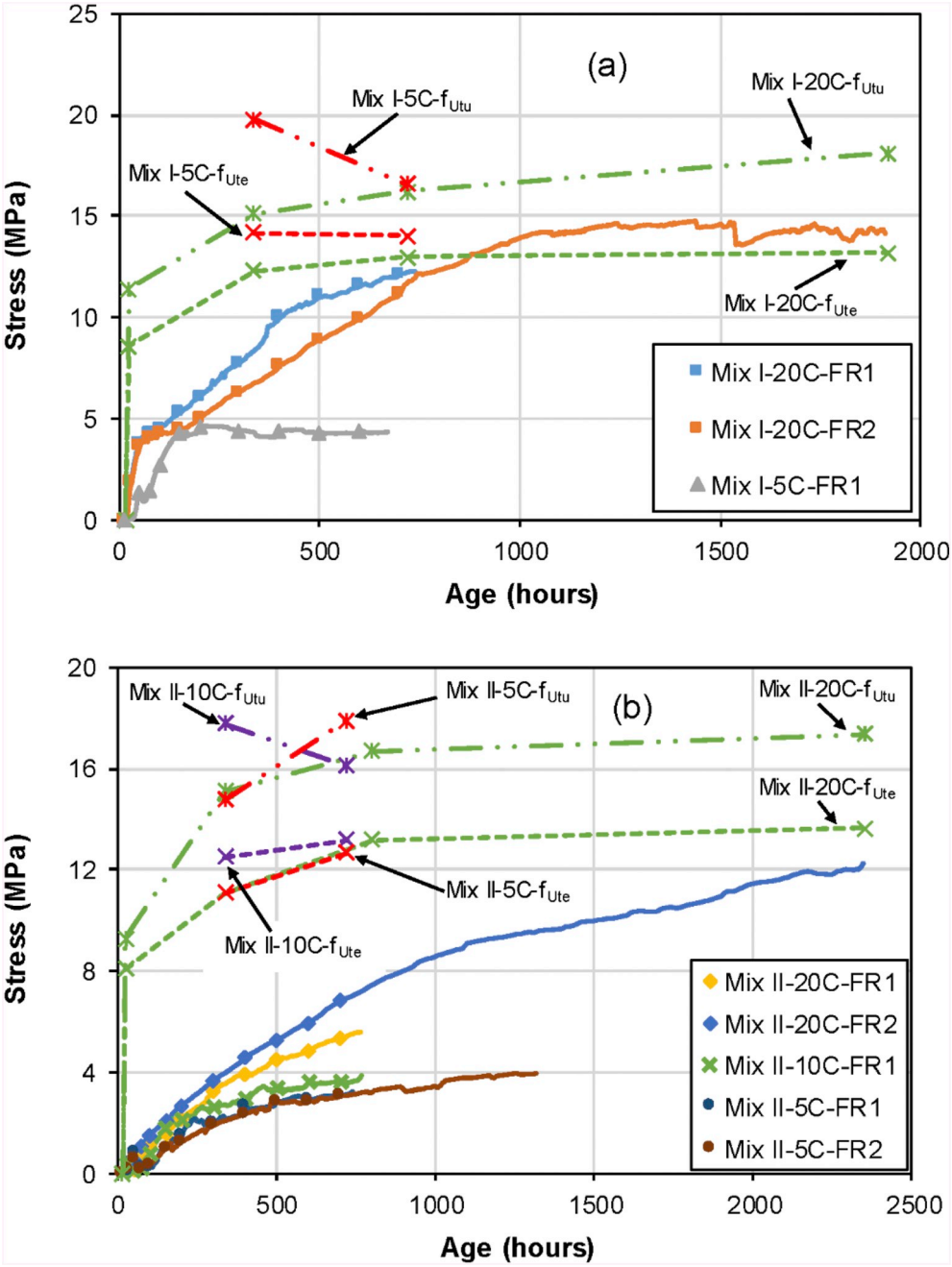

Fig. 22. Comparison of the eigenstresses developed under full restraint with the resistance curves of elastic limit and tensile strength for (a) Mix I and (b) Mix II.

the α_{cem} is about 0.08 and 0.14 for Mix I and II, respectively, whereas the corresponding α_{SF} is about 0.05 and 0.02. Therefore, the contribution of silica fume in the pozzolanic reaction is much less in zone I and the main source of autogenous shrinkage arises from the degree of hydration of the cement particles. The main contribution of the silica fume in this zone is the filler effect, thereby refining the microstructure of the mixes and influencing the self-desiccation. The case is similar for the development of eigenstresses, wherein the influence of hydration of the cement is more than that of the silica fume. The reduced eigenstresses in the Mix II, when compared to Mix I, may originate from a higher relaxation potential of Mix II as discussed earlier. Moreover, a slight decrease in the autogenous deformation of Mix II also led to a decrease in the eigenstresses, as can be more clearly seen in Fig. 20b.

4.3. Zone II

In this zone, Fig. 25a shows a deviation in the rate of development of overall degree of reaction for the mixes. Initially, Mix I shows a higher rate of development until about 70 h after which the trend is reversed until the end of Zone II. At the end of zone II (approximately 200 h), the degree of reaction becomes almost similar for both mixes. The same trend is seen in the case of elastic modulus as well, which was attributed to the higher w/c ratio in Mix II as discussed in detail in Section 3.3 and Appendix B. If it is assumed that a higher elastic modulus of Mix I in zone II is caused by more hydration products, then it implies that the pore structure of Mix I in zone II is finer than that of Mix II. A finer pore structure may lead to higher capillary stress and in

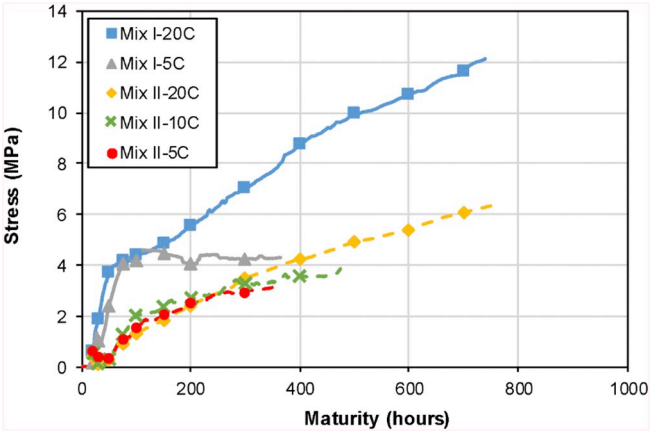

Fig. 23. Comparison of the average eigenstresses development at different quasi-isothermal temperatures for Mix I and II in the maturity domain.

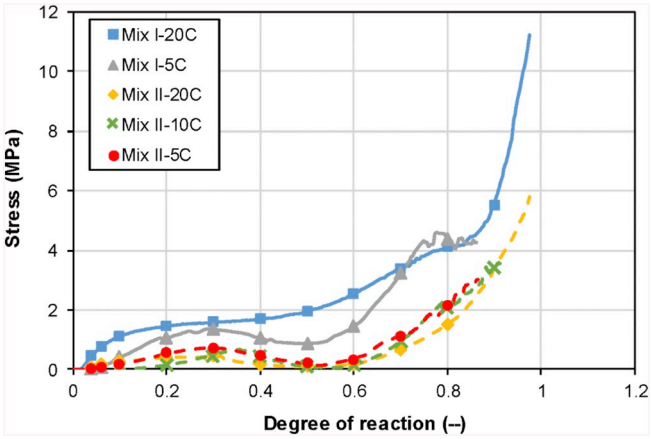

Fig. 24. Comparison of the average eigenstresses development at different quasi-isothermal temperatures for Mix I and II in the DOR domain.

turn, a higher autogenous shrinkage which is similar to what was observed experimentally in the TSTM as shown in Fig. 25f. It is also interesting to note that when the elastic modulus merges at the end of zone II, the autogenous shrinkage in both mixes also becomes similar, giving an indication that the pore structure may be identical at a similar elastic modulus. The development of eigenstresses in zone II for Mix I is somewhat stabilized whereas in the case of Mix II, it is slowly rising continuously. The trend is similar to the development of α_{cem} and the autogenous shrinkage for the respective mixes in this zone.

4.4. Zone III

In the zone III, the overall degree of hydration is still rising slowly. Even though, the relative contributions of α_{cem} in this zone are much less when compared to the previous zones, and there is a marked increase in the consumption of silica fume for the pozzolanic reaction, which is indicated by the higher rate of development of α_{SF}. This will lead to a further refinement of the microstructure. The autogenous shrinkage shows an increase in the rate of development from the beginning of zone III, which may be attributed to the finer pore structure because of the pozzolanic reaction. The eigenstresses also follow the same trend of the autogenous shrinkage, although with lesser change of rate in Mix II.

5. Conclusions

The influence of three curing temperatures, 20 °C, 10 °C and 5 °C, on the development of hydration and mechanical properties, and the development of autogenous deformations and eigenstresses under full restraint conditions were investigated for two types of SH-UHPFRC mixes with silica fume. Mix I with pure type I cement and Mix II with 50% replacement of cement with limestone filler, both having a similar steel fibrous mix. The following findings have been made in the present study.

- Using the master curve method on the cumulative heat of hydration curves at different temperatures obtained from the isothermal calorimetry tests, the activation energy E_a/R of Mix I and II were found to be 3300 K and 4000 K, respectively. It was found that, except for the autogenous shrinkage, a single activation energy could be used to include the effect of different curing temperatures on the overall degree of hydration and dynamic elastic modulus of both mixes in a maturity domain.
- Using a 'Double Danish model', the ultimate degrees of hydration of Mix I and Mix II were found to be 0.29 and 0.51, respectively.
- Using ^{29}Si MAS NMR, the degree of hydration of cement (alite and belite) and the percentage of silica fume consumed in the pozzolanic reactions were determined. The trends of α_{SF}/α_{cem} revealed that there might be two phases of pozzolanic reaction with different rates of consumptions of the silica fume. The trends also revealed that it was the heat produced from the second phase of the pozzolanic reaction that was represented by the second term of the Double Danish model.
- A systematic increase in the autogenous shrinkage was observed as the curing temperatures increased, which was attributed to greater thermal activation at higher temperature. The trend of development of autogenous shrinkage in the degree of reaction domain revealed three separate domains for both mixes; a positive rate of development until a DOR of about 0.2–0.3 followed by a zero or negative rate of development until a DOR of 0.6, which was further followed by a positive rate of development.
- The development of eigenstresses also followed the same trend as that of the autogenous shrinkage with higher stresses being developed at higher curing temperatures. The curves of the development of eigenstresses under different curing conditions almost merged in the degree of reaction domain. The eigenstresses developed were much lower in the case of Mix II, owing to its greater relaxation potential.
- It was shown that except for Mix I cured at 20 °C, the eigenstresses in none of the other tests reached the resistance envelope of the elastic limit or the tensile strength, even under full restraint conditions, during the duration of the tests. For Mix II cured at 20 °C, the eigenstresses were only approaching the strain hardening domain even at the end of three months. This ensures that, unless in the case of a detrimental fiber orientation, eigenstresses developed due to restrained shrinkage may never lead to the formation of localized macrocracks even at very low temperatures.
- The influence of the development of degree of hydration of cement and the reaction of silica fume for pozzolanic reaction on the development of autogenous shrinkage and eigenstresses were discussed. It was shown that the delayed pozzolanic reaction of silica fume at a later age, might lead to further refinement of the pore structure of the materials, leading to a further increase in the rate of development of the autogenous shrinkage and eigenstresses.

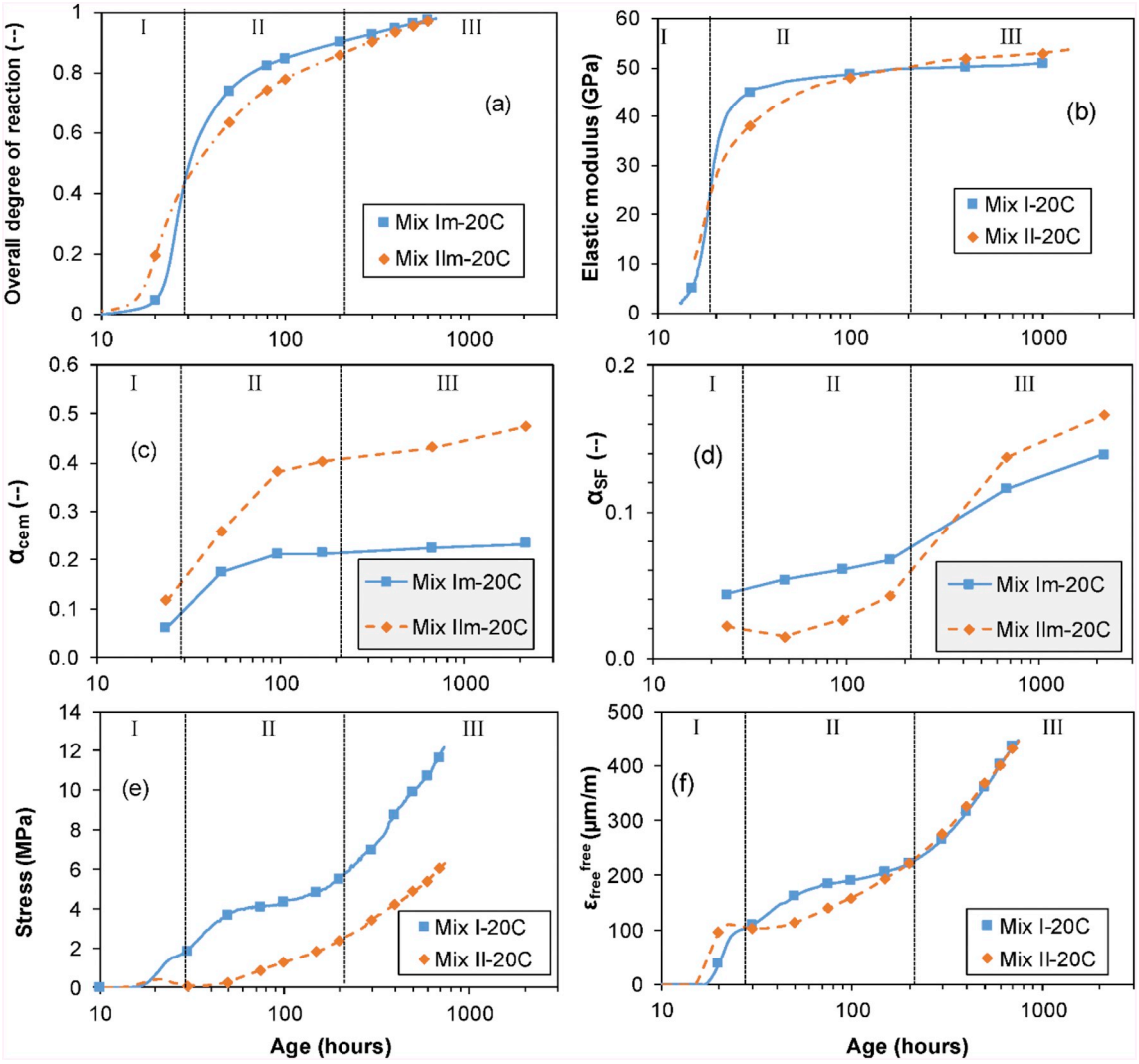

Fig. 25. Comparison of the trends observed at the material level and the structural level. Material level: (a) development of degree of reaction from the isothermal calorimetry tests, (b) development of elastic modulus from VRF tests, (c) development of α_{cem} from ^{29}Si MAS NMR, and (d) development of α_{SF} from ^{29}Si MAS NMR. Structural level: (e) development of eigenstresses under full restraint in the TSTM and (f) development of autogenous deformations zeroed after swelling in the TSTM (All the tests were carried out at a curing temperature of 20 °C).

Declaration of competing interest

The authors declare that they have no known competing financial interests or personal relationships that could have appeared to influence the work reported in this paper.

Acknowledgements

The project was financially supported by the Swiss National Science Foundation (grant 200021_153394/1). The authors would like to gratefully acknowledge the help given by the technicians of GIC-ENAC-EPFL Mr. S. Despont, Mr. G. Guignet and Mr. S. Demierre and Mr. A. Hajiesmaeili in performing the experimental works in the GIS laboratory in EPFL. The authors would also like to acknowledge the help given by Ms. Y. Briki, Mr. L. Sofia and Mr. J. D. Rego in conducting the isothermal calorimetry tests at LMC/EPFL. Mix II was developed by Mr. A. Hajiesmaeili.

Appendix A

The relative ^{29}Si NMR intensities (I) and degrees of hydration (H) for alite and belite and the percentage of silica fume reacted (α_{SF}) from the deconvolutions of the ^{29}Si MAS NMR spectra of Mix I_m and Mix II_m at different temperatures are shown in Tables A1 and A2, respectively.

Table A1
Data from the deconvolutions of the ^{29}Si MAS NMR spectra of Mix Im at different ages of hydration and cured at different temperatures.

Temp	Age (days)	I(belite)	I(alite)	I(C-S-H)	I(SF)	H(belite)	H(alite)	α_{cem}	α_{SF}
	Anhydrous	3.40	37.0		59.6				
20 °C	1	3.28	34.7	5.1	57.0	3.5	6.2	6.0	4.4
	2	3.16	30.3	10.1	56.4	7.1	18.1	17.4	5.4
	4	3.09	28.9	12.1	56.0	9.1	21.9	21.1	6.0
	7	3.15	28.8	12.5	55.6	7.4	22.2	21.2	6.7
	28	3.20	28.3	15.8	52.7	5.9	23.5	22.4	11.6
	90	3.15	28.0	17.6	51.3	7.4	24.3	23.2	13.9
10 °C	1	3.40	36.7	1.4	58.5	0.0	0.8	0.8	1.9
	2	3.39	33.9	6.1	56.7	0.3	8.4	7.9	4.9
	7	3.32	32.0	9.1	55.6	2.4	13.5	12.8	6.7
	28	3.33	31.0	11.4	54.9	2.1	16.2	15.3	7.9
5 °C	1	3.33	36.6	0.8	59.3	2.1	1.1	1.1	0.5
	2	3.39	34.7	3.4	58.5	0.3	6.2	5.8	1.9
	4	3.36	32.8	6.2	57.7	1.2	11.4	10.7	3.2
	7	3.46	29.2	10.4	56.9	1.8	21.1	19.6	4.5
	28	3.33	28.9	13.0	54.7	2.1	21.9	20.6	8.2

Table A2
Data from the deconvolutions of the ^{29}Si MAS NMR spectra of Mix IIm at different ages of hydration and cured at different temperatures.

Temp	Age (days)	I(belite)	I(alite)	I(C-S-H)	I(SF)	H(belite)	H(alite)	α_{cem}	α_{SF}
	Anhydrous	2.81	28.7		68.5				
20 °C	1	2.57	25.3	5.1	67.0	8.5	11.8	11.6	2.2
	2	2.89	20.7	8.9	67.5	0.0	27.9	25.9	1.5
	4	2.55	17.2	13.5	66.7	9.3	40.1	38.1	2.6
	7	2.50	16.6	16.3	65.6	11.0	42.2	40.1	4.2
	28	2.51	15.7	22.7	59.1	10.7	45.3	43.0	13.7
	90	2.06	14.7	27.1	57.1	26.7	48.8	47.3	16.6
10 °C	1	2.68	27.6	2.1	67.7	4.6	3.8	3.9	1.2
	2	2.55	23.5	6.7	67.2	9.3	18.1	17.5	1.9
	28	2.57	17.7	15.3	64.5	8.5	38.3	36.4	5.8
5 °C	1	2.75	28.5	0	68.3	2.1	0.7	0.8	0.3
	2	2.58	25.4	4.9	67.1	8.2	11.5	11.3	2.0
	4	2.59	22.9	7.6	67.0	7.8	20.2	19.4	2.2
	7	2.57	20.4	10.5	66.5	8.5	28.9	27.6	2.9
	28	2.46	18.8	13.9	64.8	12.5	34.5	33.1	5.4

Appendix B

This section discusses the trend of the elastic modulus as seen in Fig. 11. At any particular temperature, the dynamic elastic moduli of Mix I and II are comparable in the beginning, whereas at around an elastic modulus of 20 GPa, the rate of development becomes much slower in Mix II, for all the curing temperatures. Moreover, the trend inverts at around an elastic modulus of 40 GPa, and the values for both mixes start converging again. At a later age, the values of elastic moduli start to become more or less similar for both mixes. The time required to reach similar values depends on the curing temperature, with the 20 °C specimens reaching similar values of elastic moduli at around 180 h and the 5 °C specimens at around 3000 h. The 10 °C specimens should have had similar values between an age of 180 h and 3000 h, which was not observed in the present study, may be because of slight errors in the experimental measurements and also due to a scatter in the fiber orientation between individual test specimens.

Nevertheless, the trend of lower rate of development for Mix II at around 20 GPa and the same for Mix I at around 40 GPa could be explained by the difference in two main parameters; the silica fume/cement (SF/C) ratio and the water/cement (w/c) ratio, as discussed in [21]. Mix I has a SF/C ratio of 0.26 and Mix II has the same at 0.4, whereas the w/c ratio of Mix I is 0.163 and that of Mix II is 0.310. Jensen [25] has shown that an increase in the SF/C ratio leads to an increase in the rate of drop of relative humidity in cement paste specimens, and therefore an increase in the rate of overall hydration in the specimens. However, as shown by [14,92], only 20% mass of silica fume contributes to the pozzolanic reaction in cement based specimens. As such the difference in the effect of SF/C ratio on the trend of hydration, will be minimal in the current mixes I and II, as both of them have an SF/C ratio higher than 20%.

On the other hand, Jensen [25] has also shown a similar trend of increase in the drop of relative humidity with a decrease in the w/c ratio in the cement paste samples. Even though the drop in relative humidity is much faster in the beginning as the w/c ratio decreases, the ultimate value of the relative humidity becomes more or less similar for paste specimens with w/c < 0.3. This trend in the drop in relative humidity is analogous to the development of elastic moduli in the present case with Mix I with lower w/c ratio showing a much faster development in the beginning, but ultimately having similar values as that of Mix II with a w/c ratio of 0.310. More details regarding the discussion can be found in [21].

References

[1] E. Denarié, E. Brühwiler, Cast-on site UHPFRC for improvement of existing structures – achievements over the last 10 years in practice and research, High Perform. Fiber Reinf. Cem. Compos, 7 2015, pp. 473–480.

[2] K. Wille, S. El-Tawil, A.E. Naaman, Properties of strain hardening ultra high performance fiber reinforced concrete (UHP-FRC) under direct tensile loading, Cem.

Concr. Compos. 48 (2014) 53–66, https://doi.org/10.1016/j.cemconcomp.2013.12.015.
[3] M. Bastien-Masse, E. Denarié, E. Brühwiler, Effect of fiber orientation on the in-plane tensile response of UHPFRC reinforcement layers, Cem. Concr. Compos. 67 (2016) 111–125, https://doi.org/10.1016/j.cemconcomp.2016.01.001.
[4] K. Habel, Structural Behavior of Elements Combining Ultra-High Performance Fiber Reinforced Concretes (UHPFRC) and Reinforced Concrete, Doctoral thesis No: 3036 Ecole Polytechnique Fédérale de Lausanne, Switzerland, 2004.
[5] A. Kamen, E. Denarié, H. Sadouki, E. Brühwiler, Thermo-mechanical response of UHPFRC at early age - experimental study and numerical simulation, Cem. Concr. Res. 38 (2008) 822–831, https://doi.org/10.1016/J.CEMCONRES.2008.01.009.
[6] A. Kamen, E. Denarié, H. Sadouki, E. Brühwiler, UHPFRC tensile creep at early age, Mater. Struct. 42 (2008) 113–122, https://doi.org/10.1617/s11527-008-9371-0.
[7] A. Kamen, E. Denarié, E. Brühwiler, Thermal effects on physico-mechanical properties of ultra-high-performance fiber-reinforced concrete, ACI Mater. J. 104 (2007) 415–423.
[8] A. Kamen, E. Denarié, H. Sadouki, E. Brühwiler, Evaluation of UHPFRC activation energy using empirical models, Mater. Struct. 42 (2009) 527–537, https://doi.org/10.1617/s11527-008-9400-z.
[9] A. Switek-Rey, E. Denarié, E. Brühwiler, Early age creep and relaxation of UHPFRC under low to high tensile stresses, Cem. Concr. Res. 83 (2016) 57–69.
[10] AFNOR, 2016 NF P18-470 - Concrete - Ultra-High Performance Fiber Reinforced Concrete - Specifications, Performance, Production and Conformity, Paris, France, (2016).
[11] M.A. Hafiz, E. Denarié, Tensile response of UHPFRC under very low strain rates and low temperatures, Submitt. To Cem. Concr. Res, 2019.
[12] E. Denarié, Deliverable D25b "Guidance for the Use of UHPFRC for Rehabilitation of Concrete Highway Structures,", (2006).
[13] E. Denarié, J. Silfwerbrand, H. Beushausen, Structural Behavior, Bond. Cem. Mater. Overlays Repair, Lining or Strength. Slabs or Pavements, Springer, 2011, pp. 81–106.
[14] M. Kazemi Kamyab, Autogenous Shrinkage and Hydration Kinetics of SH-UHPFRC Under Moderate to Low Temperature Curing Conditions, Doctoral thesis No: 5681 Ecole Polytechnique Fédérale de Lausanne, Switzerland, 2013.
[15] A.M. Soliman, M.L. Nehdi, Effect of drying conditions on autogenous shrinkage in ultra-high performance concrete at early-age, Mater. Struct. 44 (2011) 879–899, https://doi.org/10.1617/s11527-010-9670-0.
[16] P. Schiessl, K. Beckhaus, I. Schachinger, P. Rucker, New results on early-age cracking risk of special concrete, Cem. Concr. Aggregates. 26 (2004) 1–9.
[17] I. Schachinger, K. Schmidt, D. Heinz, P. Schießl, Early-age cracking risk and relaxation by restrained autogenous deformation of ultra high performance concrete, 6th Int. Symp. High Strength/High Perform. Concr., Leipzig, Germany, 2002, pp. 1341–1354.
[18] A. Kamen, Comportement au jeune âge et différé d'un BFUP écrouissant sous les effets thermomécaniques, Doctoral thesis No: 3827 Ecole Polytechnique Fédérale de Lausanne, Switzerland, 2007.
[19] D.Y. Yoo, J.-J. Park, S.-W. Kim, Y.-S. Yoon, Influence of ring size on the restrained shrinkage behavior of ultra high performance fiber reinforced concrete, Mater. Struct. 47 (2014) 1161–1174, https://doi.org/10.1617/s11527-013-0119-0.
[20] D.-Y. Yoo, N. Banthia, Y.-S. Yoon, Geometrical and boundary condition effects on restrained shrinkage behavior of UHPFRC slabs, KSCE J. Civ. Eng. 22 (2018) 185–195, https://doi.org/10.1007/s12205-017-0587-9.
[21] M.A. Hafiz, A. Hajiesmaeili, E. Denarié, Tensile response of low clinker UHPFRC subjected to fully restrained shrinkage, Cem. Concr. Res. 124 (2019) 105804.
[22] L. Sorelli, R. Davila, F. Ulm, V. Perry, P. Seibert, Risk analysis of early-age cracking in UHPC structures, Proc. 2nd Int. Symp. UHPC, Kassel, Ger, 2008, pp. 331–338.
[23] M.A. Hafiz, E. Denarié, Tensile viscous response of strain hardening UHPFRC under high restraint and isothermal conditions, Euro C - 2018 Comput. Model. Concr. Struct, 2018, pp. 903–912.
[24] C. Hua, P. Acker, A. Ehrlacher, Analyses and models of the autogenous shrinkage of hardening cement paste: I. Modelling at macroscopic scale, Cem. Concr. Res. 25 (1995) 1457–1468.
[25] O.M. Jensen, Autogenous Phenomena in Cement-Based Materials, Doctoral thesis Technical University of Denmark, 2005.
[26] D.P. Bentz, O.M. Jensen, Mitigation strategies for autogenous shrinkage cracking, Cem. Concr. Compos. 26 (2004) 677–685, https://doi.org/10.1016/S0958-9465(03)00045-3.
[27] P. Acker, Swelling, shrinkage and creep: a mechanical approach to cement hydration, Mater. Struct. 37 (2004) 237–243, https://doi.org/10.1007/BF02480632.
[28] G. Sant, P. Lura, J. Weiss, The influence of temperature on unrestrained volume changes in cementitious materials, Concr. Durab. Serv. Life Plan. – Concr, 2009, pp. 538–546.
[29] G. Sant, The influence of temperature on autogenous volume changes in cementitious materials containing shrinkage reducing admixtures, Cem. Concr. Compos. 34 (2012) 855–865, https://doi.org/10.1016/j.cemconcomp.2012.04.003.
[30] A. Aili, M. Vandamme, J.-M. Torrenti, B. Masson, Is long-term autogenous shrinkage a creep phenomenon induced by capillary effects due to self-desiccation? Cem. Concr. Res. 108 (2018) 186–200, https://doi.org/10.1016/J.CEMCONRES.2018.02.023.
[31] O.M. Jensen, P.F. Hansen, Influence of temperature on autogenous deformation and relative humidity change in hardening cement paste, Cem. Concr. Res. 29 (1999) 567–575, https://doi.org/10.1016/S0008-8846(99)00021-6.
[32] P. Turcry, A. Loukili, L. Barcelo, J.M. Casabonne, Can the maturity concept be used to separate the autogenous shrinkage and thermal deformation of a cement paste at early age? Cem. Concr. Res. 32 (2002) 1443–1450, https://doi.org/10.1016/S0008-8846(02)00800-1.
[33] G. Sant, B. Lothenbach, P. Juilland, G. Le Saout, J. Weiss, K. Scrivener, The origin of early age expansions induced in cementitious materials containing shrinkage reducing admixtures, Cem. Concr. Res. 41 (2011) 218–229.
[34] C. Jiang, Y. Yang, Y. Wang, Y. Zhou, C. Ma, Autogenous shrinkage of high performance concrete containing mineral admixtures under different curing temperatures, Constr. Build. Mater. 61 (2014) 260–269, https://doi.org/10.1016/j.conbuildmat.2014.03.023.
[35] P. Lura, K. van Breugel, I. Maruyama, Effect of curing temperature and type of cement on early-age shrinkage of high-performance concrete, Cem. Concr. Res. 31 (2001) 1867–1872, https://doi.org/10.1016/S0008-8846(01)00601-9.
[36] Ç. Yalçınkaya, H. Yazıcı, Effects of ambient temperature and relative humidity on early-age shrinkage of UHPC with high-volume mineral admixtures, Constr. Build. Mater. 144 (2017) 252–259, https://doi.org/10.1016/j.conbuildmat.2017.03.198.
[37] E. Gallucci, X. Zhang, K.L. Scrivener, Effect of temperature on the microstructure of calcium silicate hydrate (C-S-H), Cem. Concr. Res. 53 (2013) 185–195, https://doi.org/10.1016/j.cemconres.2013.06.008.
[38] I. Pane, W. Hansen, Investigation of blended cement hydration by isothermal calorimetry and thermal analysis, Cem. Concr. Res. 35 (2005) 1155–1164, https://doi.org/10.1016/j.cemconres.2004.10.027.
[39] K.O. Kjellsen, R.J. Detwiler, O.E. Gjørv, Development of microstructures in plain cement pastes hydrated at different temperatures, Cem. Concr. Res. 21 (1991) 179–189, https://doi.org/10.1016/0008-8846(91)90044-I.
[40] J.I. Escalante-García, J.H. Sharp, Effect of temperature on the hydration of the main clinker phases in Portland cements: part i, neat cements, Cem. Concr. Res. 28 (1998) 1245–1257, https://doi.org/10.1016/S0008-8846(98)00115-X.
[41] J.I. Escalante-García, J.H. Sharp, Effect of temperature on the hydration of the main clinker phases in Portland cements: part ii, blended cements, Cem. Concr. Res. 28 (1998) 1259–1274, https://doi.org/10.1016/S0008-8846(98)00107-0.
[42] B. Lothenbach, F. Winnefeld, C. Alder, E. Wieland, P. Lunk, Effect of temperature on the pore solution, microstructure and hydration products of Portland cement pastes, Cem. Concr. Res. 37 (2007) 483–491, https://doi.org/10.1016/j.cemconres.2006.11.016.
[43] I. Elkhadiri, M. Palacios, F. Puertas, Effect of curing temperature on cement hydration, Ceram. - Silikaty. 53 (2009) 65–75.
[44] K.O. Kjellsen, R.J. Detwiler, Reaction kinetics of Portland cement mortars hydrated at different temperatures, Cem. Concr. Res. 22 (1992) 112–120, https://doi.org/10.1016/0008-8846(92)90141-H.
[45] P. Rossi, J.P. Charron, M. Bastien-Masse, J.L. Tailhan, F. Le Maou, S. Ramanich, Tensile basic creep versus compressive basic creep at early ages: comparison between normal strength concrete and a very high strength fiber reinforced concrete, Mater. Struct. 47 (2014) 1773–1785.
[46] A. Loukili, P. Richard, J. Lamirault, A study on delayed deformations of an ultra high strength Cementitious material, Spec. Publ. 179 (1998) 929–950.
[47] M. Cheyrezy, M. Behloul, Creep and shrinkage of ultra-high performance concrete, Creep, Shrinkage Durab. Mech. Concr. Other Quasi-Brittle Mater. (Concreep 6), 2001, pp. 527–538.
[48] V.Y.Y. Garas, K.E.E. Kurtis, L.F.F. Kahn, Creep of UHPC in tension and compression: effect of thermal treatment, Cem. Concr. Compos. 34 (2012) 493–502, https://doi.org/10.1016/J.CEMCONCOMP.2011.12.002.
[49] Y. Xu, J.J. Liu, J.J. Liu, P. Zhang, Q. Zhang, L. Jiang, Experimental studies and modeling of creep of UHPC, Constr. Build. Mater. 175 (2018) 643–652, https://doi.org/10.1016/J.CONBUILDMAT.2018.04.157.
[50] A.E. Switek, Time-Dependent Response of Ultra High Performance Fiber Reinforced Concrete (UHPFRC) under Low to High Tensile Stresses, Doctoral thesis No: 4899 Ecole Polytechnique Fédérale de Lausanne, Switzerland, 2011.
[51] V.Y. Garas, L.F. Kahn, K.E. Kurtis, Short-term tensile creep and shrinkage of ultra-high performance concrete, Cem. Concr. Compos. 31 (2009) 147–152, https://doi.org/10.1016/J.CEMCONCOMP.2009.01.002.
[52] V.Y. Garas, A.R. Jayapalan, L.F. Kahn, K.E. Kurtis, Micro- and Nanoscale characterization of effect of interfacial transition zone on tensile creep of ultra-high-performance concrete, Transp. Res. Rec. 2141 (2010) 82–88, https://doi.org/10.3141/2141-14.
[53] A. Switek-Rey, E. Denarié, E. Brühwiler, Tensile creep of UHPFRC under low and high stresses, 4th Int. Conf. Constr. Mater. – Performance, Innov. Struct. Implic., Nagoya, Japan, 2009, pp. 432–437.
[54] K. Habel, J.P. Charron, E. Denarié, E. Brühwiler, Autogenous deformations and viscoelasticity of UHPFRC in structures. Part I: experimental results, Mag. Concr. Res. 58 (2006) 135–145.
[55] A. Switek-Rey, E. Denarié, E. Brühwiler, Early age creep and relaxation of UHPFRC under low to high tensile stresses, Cem. Concr. Res. 83 (2016) 57–69, https://doi.org/10.1016/J.CEMCONRES.2016.01.005.
[56] P. Acker, M. Behloul, Ductal technology: a large spectrum of properties, a wide range of applications, Proc. Int. Symp. Ultra High Perform. Concr., Kassel, Germany, 2004, pp. 11–23.
[57] S. Utsi, J.-E. Jonasson, Estimation of the risk for early thermal cracking for SCC containing fly ash, Mater. Struct. 45 (2012) 153–169, https://doi.org/10.1617/s11527-011-9757-2.
[58] G. Ji, Cracking Risk of Concrete Structures in the Hardening Phase: Experiments, Material Modeling and Finite Element Analysis, Doctoral Thesis Norwegian University of Science and Technology, 2008.
[59] I. Mehdipour, K.H. Khayat, Elucidating the role of supplementary cementitious materials on shrinkage and restrained-shrinkage cracking of flowable eco-concrete, J. Mater. Civ. Eng. ASCE. 30 (2018).
[60] K. Kuder, D. Lehman, J. Berman, G. Hannesson, R. Shogren, Mechanical properties of self consolidating concrete blended with high volumes of fly ash and slag, Constr. Build. Mater. 34 (2012) 285–295, https://doi.org/10.1016/j.conbuildmat.2012.02.

034.
[61] B.A. Gedam, N.M. Bhandari, A. Upadhyay, Influence of supplementary cementitious materials on shrinkage, creep, and durability of high-performance concrete, J. Mater. Civ. Eng. 28 (4015173) (2016) 1–11, https://doi.org/10.1061/(ASCE)MT.1943-5533.0001462.
[62] W.S. Langley, G.G. Carette, V.M. Malhotra, Structural concrete incorporating high volumes of ASTM class fly ash, Mater. J. 86 (1989) 507–514.
[63] V. Sivasundaram, G.G. Carette, V.M. Malhotra, Mechanical properties, creep, and resistance to diffusion of chloride ions of concretes incorporating high volumes of ASTM class F fly ashes from seven different sources, Mater. J. 88 (1991) 407–416.
[64] G.G. Carette, V.M. Malhotra, Characterization of Canadian fly ashes and their relative performance in concrete, Can. J. Civ. Eng. 14 (1987) 667–682.
[65] P. Rossi, A. Arca, E. Parant, P. Fakhri, Bending and compressive behaviors of a new cement composite, Cem. Concr. Res. 35 (2005) 27–33, https://doi.org/10.1016/J.CEMCONRES.2004.05.043.
[66] E. Denarié, K. Habel, J. Wuest, SAMARIS Deliverable D13, Report on Preliminary Studies for the Use of HPFRCC for the Rehabilitation of Road Infrastructure Components, http://samaris.zag.si, (2004).
[67] E. Denarié, Recommendations for the Tailoring of UHPFRC Recipes for Rehabilitation, Deliverable ARCHES D06, http://arches.fehrl.org, (2009).
[68] SIA, Cahier Technique 2052, Béton fibré ultra-performant (BFUP): Matériaux, dimensionnement et exécution, SIA, Zürich, 2017 (2017).
[69] L. Wadsö, Operational issues in isothermal calorimetry, Cem. Concr. Res. 40 (2010) 1129–1137, https://doi.org/10.1016/j.cemconres.2010.03.017.
[70] K. Scrivener, R. Snellings, B. Lothenbach, A Practical Guide to Microstructural Analysis of Cementitious Materials, Crc Press, 2018.
[71] J. Skibsted, H.J. Jakobsen, C. Hall, Quantification of calcium silicate phases in Portland cements by ^{29}Si MAS NMR spectroscopy, J. Chem. Soc. Faraday Trans. 91 (1995) 4423–4430, https://doi.org/10.1039/FT9959104423.
[72] S.L. Poulsen, V. Kocaba, G. Le Saoût, H.J. Jakobsen, K.L. Scrivener, J. Skibsted, Improved quantification of alite and belite in anhydrous Portland cements by ^{29}Si MAS NMR: effects of paramagnetic ions, Solid State Nucl. Magn. Reson. 36 (2009) 32–44, https://doi.org/10.1016/j.ssnmr.2009.05.001.
[73] J. Skibsted, M.D. Andersen, The effect of alkali ions on the incorporation of aluminum in the calcium silicate hydrate (C–S–H) phase resulting from Portland cement hydration studied by ^{29}Si MAS NMR, J. Am. Ceram. Soc. 96 (2013) 651–656, https://doi.org/10.1111/jace.12024.
[74] Z. Dai, T.T. Tran, J. Skibsted, Aluminum incorporation in the C–S–H phase of white Portland cement–metakaolin blends studied by ^{27}Al and ^{29}Si MAS NMR spectroscopy, J. Am. Ceram. Soc. 97 (2014) 2662–2671, https://doi.org/10.1111/jace.13006.
[75] S. Kolluru, J. Popovics, S.P. Shah, Determining elastic properties of concrete using vibrational resonance frequencies of standard test cylinders, Cem. Concr. Aggregates. 22 (2000) 81.
[76] SIA 262/1:2013, Construction en Beton Specifications Complementaires, (2013).
[77] O. Bjontegaard, Thermal Dilatation and Autogenous Deformation as Driving Forces to Self-Induced Stresses in High Performance Concrete, Doctoral thesis The University of Trondheim, Norway, 1999.
[78] J.P. Charron, J. Marchand, M. Pigeon, B. Bissonnette, Test device for studying the early-age stresses and strains in concrete, Spec. Publ. 220 (2004) 113–124, https://doi.org/10.14359/13153.
[79] K. Kovler, Testing system for determining the mechanical behavior of early age concrete under restrained and free uniaxial shrinkage, Mater. Struct. 27 (1994) 324–330.
[80] E. Berodier, K. Scrivener, Understanding the filler effect on the nucleation and growth of C-S-H, J. Am. Ceram. Soc. 97 (2014) 3764–3773, https://doi.org/10.1111/jace.13177.
[81] A. Bazzoni, Study of Early Hydration Mechanisms of Cement by Means of Electron Microscopy, Doctoral Thesis no: 6296, EPFL, Switzerland, 2014.
[82] J.I. Escalante-Garcia, J.H. Sharp, The effect of temperature on the early hydration of Portland cement and blended cements, Adv. Cem. Res. 12 (2000) 121–130.
[83] M.T. Palou, E. Kuzielová, M. Žemlička, M. Boháč, R. Novotný, The effect of curing temperature on the hydration of binary Portland cement, J. Therm. Anal. Calorim. 125 (2016) 1301–1310, https://doi.org/10.1007/s10973-016-5395-9.
[84] C. Angulski da Luz, H. R. D, Influence of curing temperature on the process of hydration of supersulfated cements at early age, Cem. Concr. Res. 77 (2015) 69–75, https://doi.org/10.1016/j.cemconres.2015.07.002.
[85] F. Han, Z. Zhang, D. Wang, P. Yan, Hydration kinetics of composite binder containing slag at different temperatures, J. Therm. Anal. Calorim. 121 (2015) 815–827, https://doi.org/10.1007/s10973-015-4631-z.
[86] B. Klemczak, M. Batog, Heat of hydration of low-clinker cements, J. Therm. Anal. Calorim. 123 (2016) 1351–1360, https://doi.org/10.1007/s10973-015-4782-y.
[87] P.F.G. Banfill, Superplasticizers for Ciment Fondu. Part 2: effects of temperature on the hydration reactions, Adv. Cem. Res. 7 (1995) 151–157, https://doi.org/10.1680/adcr.1995.7.28.151.
[88] L. D'Aloia, G. Chanvillard, Determining the "apparent" activation energy of concrete: Ea—numerical simulations of the heat of hydration of cement, Cem. Concr. Res. 32 (2002) 1277–1289, https://doi.org/10.1016/S0008-8846(02)00791-3.
[89] E. Wirquin, M. Broda, B. Duthoit, Determination of the apparent activation energy of one concrete by calorimetric and mechanical means: influence of a superplasticizer, Cem. Concr. Res. 32 (2002) 1207–1213, https://doi.org/10.1016/S0008-8846(02)00770-6.
[90] F.P. Hansen, E.J. Pedersen, Maturity computer for controlled curing and hardening of concrete, Nord. Betong 1 (1977) 21–25.
[91] E. Denarié, Internal Communication, MCS, EPFL, Switzerland, 2012.
[92] V. Waller, Relations entre composition des bétons, exothermie en cours de prise et résistance à la compression, thèse de doctorat LCPC, Nantes, France, 2001.
[93] O.M. Jensen, P.F. Hansen, Water-entrained cement-based materials: I. Principles and theoretical background, Cem. Concr. Res. 31 (2001) 647–654, https://doi.org/10.1016/S0008-8846(01)00463-X.
[94] P. Lura, O.M. Jensen, K. van Breugel, Autogenous shrinkage in high-performance cement paste: an evaluation of basic mechanisms, Cem. Concr. Res. 33 (2003) 223–232.
[95] W.J. Weiss, P. Lura, F. Rajabipour, G. Sant, Performance of shrinkage-reducing admixtures at different humidities and at early ages, Mater. J. 105 (5) (2008) 478–486, https://doi.org/10.14359/19977.
[96] W. Huang, H. Kazemi-Kamyab, W. Sun, K. Scrivener, Effect of cement substitution by limestone on the hydration and microstructural development of ultra-high performance concrete (UHPC), Cem. Concr. Compos. 77 (2017) 86–101, https://doi.org/10.1016/j.cemconcomp.2016.12.009.